Triangular and quadrilateral 2D linked-interpolation finite elements for micropolar continuum

Sara Grbčić[a,b,*], Gordan Jelenić[a], Dragan Ribarić[a]

[a] *University of Rijeka, Faculty of Civil Engineering, Croatia*
[b] *Université de Technologie de Compiègne / Sorbonne Universités, France*

Abstract

Triangular and quadrilateral finite elements for linear micropolar continuum theory are developed using linked interpolation. In order to satisfy convergence criteria, the newly presented finite elements are modified using the Petrov-Galerkin method in which different interpolation is used for the test and trial functions. The elements are tested through four numerical examples consisting of a set of patch tests, a cantilever beam in pure bending and a stress concentration problem and compared with the analytical solution and membrane micropolar finite elements with standard Lagrangian interpolation. In the higher-order patch test, the performance of the first-order element is visibly improved, significantly so for the quadrilateral elements. All the presented elements also faithfully reproduce the micropolar effects in the stress concentration analysis, but the enhancement is here negligible with respect to standard Lagrangian elements.

Keywords: micropolar theory, finite element method, linked interpolation, membrane elements

*Corresponding author
Email addresses: sara.grbcic@uniri.hr (Sara Grbčić), gordan.jelenic@uniri.hr (Gordan Jelenić), dragan.ribaric@uniri.hr (Dragan Ribarić)

1. Introduction

The commonly used Cauchy's continuum theory (the *classical* theory) in most cases faithfully reproduces experimental results, in particular those carried out on highly homogeneous construction materials such as steel and aluminium, but discrepancies between theory and experiments are at times still observed [1]. Carefully conducted experiments on materials with granular, fibrous or lattice structure show that such materials cannot be adequately modelled using the classical continuum theory. Commonly, in regions of high stress gradients, such as the neighbourhoods of holes, notches and cracks, the stress concentration factor as predicted by the classical theory is higher than that observed experimentally. In addition, it sometimes turns out to be independent of the size of the imperfection that causes it, which also does not correspond to the experimental observations. There exist specimens, e.g. rods made of foam subject to torsion and bending, in which the size effect is clearly observed [2], which is again inconsistent with the classical continuum theory. In addition, the classical continuum theory strictly relies on symmetry of the Cauchy stress tensor, which effectively makes it unable to accommodate arbitrary natural boundary conditions. More discrepancies between the classical continuum theory and the experimental testing may be observed in dynamics, thermal analysis and fluid mechanics [1]. In an attempt to answer to such obvious anomalies, numerous alternative continuum theories have been developed, such as the micromorphic, the microstretch, or the couple-stress continuum theory [3], to name only a few. One of such theories is the so-called *micropolar* continuum theory, usually attributed to the Cosserat brothers [4].

In the micropolar continuum theory, the interaction between material particles is described by means of not only the stress vector field, but also the *couple-stress* vector field. As a result, in addition to the stress tensor, an additional *couple-stress tensor* is obtained, and both of these tensors are *non-symmetric*. Consequently, in the micropolar continuum theory there exist two independent kinematic fields, the displacement field and the so-called *microrotation* field,

which represents the *local rotation* of a material point, which is completely independent of the so-called *macrorotation* of the classical continuum theory (the skew-symmetric part of the displacement gradient) [5]. By analysing the geometry of the deformation process, we further obtain two strain tensors, the (micropolar) *strain tensor*, in which the microrotations are present, and the so-called *curvature* tensor as the microrotation gradient energy-conjugate to the couple-stress tensor. Again, both of these tensors are non-symmetric. If we consider a material which is linear elastic, homogeneous and isotropic, it necssarily turns out to be described by *six independent material constants*, in contrast to only two constants present in a linear elastic, homogeneous and isotropic classical continuum. From a mathematical point of view, an isotropic micropolar material is a continuum in which rigid particles of infinitesimal size are uniformly distributed in an elastic matrix and in which homogeneity and isotropy are taken to be the macroproperties of the medium. The couple stresses physically originate from the bending and twisting moments transmitted between the rigid particles within the material, while the microrotation field describes their rotation.

There are evidences (see e.g. [1], [6] and [7]) that the micropolar continuum theory is in certain circumstances better suited to model the actual behaviour of a material than the classical theory. Furthermore, using the micropolar theory it is possible to model the asymmetric stress-strain analysis, in contrast to the classical theory. The importance of the material microstructure was first recognised by Voigt [8] who suggested that the interaction between material particles within a body should be assumed not only by a force vector, but also by a moment vector and was the first one to obtain the stress tensor as a non-symmetric field. Two decades later, the Cosserat brothers extended Voigt's theory and introduced the theory of non-symmetric elasticity [4]. They assumed that to each particle a rigid trihedron is attached, which can translate and rotate during the deformation process. In this way, each material particle had as many as *six* degrees of freedom: three displacement components and three rotation components. The theory was originally presented as a unified

theory which brings together mechanics, optics, magnetism and electrodynamics, but it did not provide the detail on the constitutive equations. The theory had remained dormant for nearly half a century and was reopened by Günther [9] who gave the fundamentals of the *linear* Cosserat continuum and discussed in detail the 1D, 2D and 3D models. Six years later, Truesdell and Toupin [10] present their analysis of the so-called *Cosserat pseudocontinuum* (nowadays also known as the *couple-stress continuum*), where the non-symmetric stress tensor is obtained, but the deformation is determined by the displacement vector only, using the macrorotation for the rotation field [3]. Further analysis of the *linear* Cosserat continuum was given by Schäfer [11], who focused only on the 2D case. The latest extension of the Cosserat theory was provided by Eringen [12], who included the body microinertia effects in dynamics and suggested the presently used denomination of the theory as the *micropolar* theory of elasticity. Other than Cosserat's or micropolar, this theory is in the literature also referred to as the *asymmetric* theory of elasticity.

A possible reason why the micropolar continuum theory is not widely used in the numerical analysis of structures may lie in the lack of reliable procedures to determine the material parameters. Even though there exist numerous works related to micropolar theory (see e.g. [13, 3, 14] among many others), relatively few experimental tests have been successfully conducted. An analytical and experimental procedure for determining the micropolar material constants is given in [15], but without particular success in the experimental part since an opposite trend to the prediction has been observed. The most significant contribution to devising experimental procedures to determine the micropolar material parameters is given by Lakes and co-workers in their analysis of bones [16, 17, 18], polymeric foams [19, 20, 2, 21] and metal foams [22]. A different approach to determining the micropolar parameters is based on various homogenisation procedures applied to lattices, granular media, cellular structures and heterogeneus structures such as masonry structures [23, 24, 25, 26], which provide a more significant source of the actual values for the micropolar parameters. In contrast to the above experiments performed by Lakes and his co-workers, which involve

specimen preparation on a very small scale, the idea of homogenisation is to replace a larger-scale composite material or assembly of particles by an effective micropolar continuum model. Assuming a homogeneous Cosserat material that best approximates a heterogeneous Cauchy material, the material parameters of the observed specimen may be determined more easily. A comprehensive list of related works can be found in [14].

As mentioned in [27], newer, more comprehensive material models are struggling with experimental verification and their corresponding conceptualisation and interpretation. We are faced with a situation where theory precedes experiment. Due to the lack of experimental verifications, we believe that the key to understanding and developing more precise experimental procedures lies in the comprehensive numerical analysis of the solution of a boundary value problem analysed. The numerical analysis should broaden the range of solvable problems and open up new possibilities for the numerical simulation of experimental schemes, so the development of finite elements of high quality is important in the future progress and understanding of the micropolar continuum theory.

In this paper we present membrane (triangular and quadrilateral) finite elements of different order based on the linear micropolar continuum theory containing a specific family of interpolation functions for the displacement field of arbitrary order called *linked interpolation*. The proposed family of interpolation functions are derived from the closed-form solution of the Timoshenko beam problem [28], which are later successfully applied to the Mindlin plate problem [29, 30]. This interpolation involves nodal displacements as well as nodal rotations to describe the displacement field. The derived elements will be compared to the micropolar membrane finite elements involving standard Lagrangian interpolation in four different numerical examples consisting of a force and displacement patch tests, higher-order patch tests and a stress concentration analysis.

2. Micropolar continuum model

Let us briefly outline the basic equations of the micropolar continuum theory. The detailed exposition may be found in the literature, see e.g. [1]. Let us analyse a continuous body $\mathcal{B}$ of volume V and surface S under the influence of external actions consisting of distributed volume loads $\mathbf{p}_\mathrm{v}$ and $\mathbf{m}_\mathrm{v}$ and distributed surface loads $\mathbf{p}_\mathrm{s}$ and $\mathbf{m}_\mathrm{s}$, where $\mathbf{p}_\mathrm{v}$ is a body force, $\mathbf{m}_\mathrm{v}$ a body moment, $\mathbf{p}_\mathrm{s}$ a surface force and $\mathbf{m}_\mathrm{s}$ a surface moment.

At a particular point X within the body at time t there exists a second-order tensor field $\boldsymbol{\sigma}(\mathbf{x},t)$ called the Cauchy stress tensor and an additional second-order *couple-stress tensor* $\boldsymbol{\mu}(\mathbf{x},t)$ where $\mathbf{x}$ is the position vector of the point X with respect to a chosen spatial frame of reference.

Equilibrium equations. In the state of static equilibrium, we have the following force equilibrium equation

$$\boldsymbol{\sigma}\nabla + \mathbf{p}_\mathrm{v} = \mathbf{0}, \tag{1}$$

where ∇ is the differential operator nabla, as well as the moment equilibrium equation

$$\boldsymbol{\mu}\nabla + \mathbf{a} + \mathbf{m}_\mathrm{v} = \mathbf{0}, \tag{2}$$

where $\mathbf{a}$ is twice the axial vector of the skew-symmetric part $\boldsymbol{\sigma}_\mathrm{a} = \frac{1}{2}(\boldsymbol{\sigma} - \boldsymbol{\sigma}^\mathrm{T})$ of the stress tensor, i.e.

$$\mathbf{a} = 2\mathrm{axial}(\boldsymbol{\sigma}_\mathrm{a}) \tag{3}$$

defined such that $\mathbf{a} \times \mathbf{v} = 2\boldsymbol{\sigma}_\mathrm{a}\mathbf{v}$ for any 3D vector $\mathbf{v}$. Attaching a triad of orthogonal base vectors and corresponding Cartesian co-ordinates to the chosen spatial frame of reference, equilibrium equations (1) and (2) may be written as

$$\sigma_{ij,j} + p_{v_i} = 0, \qquad \mu_{ij,j} - \varepsilon_{ijk}\sigma_{jk} + m_{v_i} = 0, \tag{4}$$

where the first index denotes the direction of the stress or axis of the couple stress with respect to the coordinate base and the second index denotes the direction of the surface normal. The summational convention on repeated indices

is implied, and a comma denotes differentiation with respect to a particular spatial coordinate, while ε_{ijk} is the permutation tensor of Levi-Civita.

Likewise, the following natural boundary conditions are defined for the part of the body surface subject to applied loading:

$$\boldsymbol{\sigma}\ \mathbf{n} = \mathbf{p}_\mathrm{s} \quad \Leftrightarrow \quad \sigma_{ij} n_j = p_{si}, \qquad\qquad \boldsymbol{\mu}\ \mathbf{n} = \mathbf{m}_\mathrm{s} \quad \Leftrightarrow \quad \mu_{ij} n_j = m_{si}, \tag{5}$$

where $\mathbf{n}$ is the outward unit normal to the surface, along with the essential boundary conditions on the part of the body surface with prescribed kinematics.

Kinematic equations. In the micropolar continuum theory we have a displacement field $\mathbf{w}(\mathbf{x})$ and an additional kinematic field $\boldsymbol{\varphi}(\mathbf{x})$ known as the microrotation field which represents the local rotation of the point X and is completely independent of the displacement field, i.e. different from the rotational part of the displacement gradient $\boldsymbol{\omega} = \frac{1}{2}\left(\mathbf{w} \otimes \nabla - \nabla \otimes \mathbf{w}\right)$ (the macrorotation of the classical continuum theory; see [5]). The *micropolar strain tensor* $\boldsymbol{\epsilon}$ is defined as

$$\boldsymbol{\epsilon} = \operatorname{grad} \mathbf{w} - \widehat{\boldsymbol{\varphi}} = \mathbf{w} \otimes \nabla - \widehat{\boldsymbol{\varphi}} \quad \Leftrightarrow \quad \epsilon_{ij} = w_{i,j} + \varepsilon_{ijk} \varphi_k, \tag{6}$$

where a superimposed hat on a vector field $(\cdot)$ denotes a skew-symmetric cross-product operator such that $\widehat{(\cdot)}\mathbf{v} = (\cdot) \times \mathbf{v}$ for any 3D vector $\mathbf{v}$. Owing to the existence of an independent rotation field $\boldsymbol{\varphi}$, there also exists a corresponding *micropolar curvature tensor*

$$\boldsymbol{\kappa} = \operatorname{grad} \boldsymbol{\varphi} = \boldsymbol{\varphi} \otimes \nabla \quad \Leftrightarrow \quad \kappa_{ij} = \varphi_{i,j}, \tag{7}$$

where the diagonal terms represent *torsional strains*. The so-callled *couple-stress* theory is a special case of the micropolar continuum theory where the microrotation vector $\boldsymbol{\varphi}$ is equal to the macrorotation vector $\boldsymbol{\omega}$ and thus *ceases to exist as an independent field*. As a consequence, in the couple-stress theory, the curvature tensor involves *second derivatives* of the dispacement field. When these derivatives are neglected, the curvature tensor also vanishes and the couple-stress theory reduces to the classical continuum theory.

Constitutive equations. In a homogeneous isotropic linear elastic micropolar continuum, the second-order stress and strain tensors $\boldsymbol{\sigma}$ and $\boldsymbol{\epsilon}$ are related via a constant isotropic fourth-order *constitutive tensor* $\mathbf{T}$ such that in the Cartesian component form we have [31]

$$\sigma_{ij} = T_{ijpq}\epsilon_{pq}, \quad T_{ijpq} = \lambda\delta_{ij}\delta_{pq} + \mu(\delta_{ip}\delta_{jq} + \delta_{iq}\delta_{jp}) + \nu(\delta_{ip}\delta_{jq} - \delta_{iq}\delta_{jp}), \quad (8)$$

where λ and μ are the Lamé constants, ν is another material constant and δ_{ij} is the Kronecker symbol. In the micropolar continuum theory the couple-stress tensor $\boldsymbol{\mu}$ is related to the curvature tensor $\boldsymbol{\kappa}$ in a completely analogous way involving three additional material constants so that eventually

$$\sigma_{ij} = \lambda\epsilon_{pp}\delta_{ij} + (\mu+\nu)\epsilon_{ij} + (\mu-\nu)\epsilon_{ji}, \qquad \mu_{ij} = \alpha\kappa_{pp}\delta_{ij} + (\beta+\gamma)\kappa_{ij} + (\beta-\gamma)\kappa_{ji}, \quad (9)$$

where $\alpha,\ \beta,\ \gamma$ are additional material parameters of the linear isotropic micropolar continuum. The following restrictions on the material parameters hold true as a consequence of positive definiteness of the constitutive tensors: $3\lambda+2\mu > 0$, $\mu > 0$, $\nu > 0$, $3\alpha + 2\beta > 0$, $\beta > 0$ and $\gamma > 0$. Note that all the stress and strain tensors are now in general non-symmetric.

These material parameters may be related to a set of technical (measurable) parameters consisting of shear modulus G, Poisson's ratio n, a dimensionless coupling number between the macrorotation and the microrotation $N \in \langle 0, 1\rangle$, a dimensionless polar ratio of rotation sensitivity (a quantity which relates the torsional strains in a way analogous to that in which Poisson's ratio relates the normal strains) $\psi \in \langle 0, \frac{3}{2}\rangle$, and the characteristic lengths for torsion and bending l_t and l_b as [32]

$$\begin{gathered} \lambda = \tfrac{2n\ G}{1-2n}, \qquad \mu = G, \qquad \nu = \tfrac{G\ N^2}{1-N^2}, \\ \alpha = \tfrac{2G\ l_t^2(1-\psi)}{\psi}, \quad \beta = G\ l_t^2, \quad \gamma = G(4l_b^2 - l_t^2). \end{gathered} \quad (10)$$

Weak form of the equilibrium equations.. To construct a numerical solution procedure of the boundary value problem analysed, it is useful to define the principle of virtual work as the weak form of the equilibrium equations, i.e. to

state that the virtual work of external forces must be equal to the virtual work of the internal forces

$$G^{int}(\mathbf{w}, \boldsymbol{\varphi}; \overline{\mathbf{w}}, \overline{\boldsymbol{\varphi}}) = G^{ext}(\overline{\mathbf{w}}, \overline{\boldsymbol{\varphi}}), \tag{11}$$

with the virtual works of internal and external forces defined as

$$\begin{aligned} G^{int}(\mathbf{w}, \boldsymbol{\varphi}; \overline{\mathbf{w}}, \overline{\boldsymbol{\varphi}}) &= \textstyle\int_V (\overline{\boldsymbol{\epsilon}} : \boldsymbol{\sigma} + \overline{\boldsymbol{\kappa}} : \boldsymbol{\mu}) dV, \\ G^{ext}(\overline{\mathbf{w}}, \overline{\boldsymbol{\varphi}}) &= \textstyle\int_V (\overline{\mathbf{w}} \cdot \mathbf{p}_{\mathrm{v}} + \overline{\boldsymbol{\varphi}} \cdot \mathbf{m}_{\mathrm{v}}) dV + \int_S (\overline{\mathbf{w}} \cdot \mathbf{p}_{\mathrm{s}} + \overline{\boldsymbol{\varphi}} \cdot \mathbf{m}_{\mathrm{s}}) dS, \end{aligned} \tag{12}$$

where $\overline{\mathbf{w}}$ and $\overline{\boldsymbol{\varphi}}$ are the virtual displacement and microrotation vectors and $\overline{\boldsymbol{\epsilon}}$ and $\overline{\boldsymbol{\kappa}}$ are the corresponding tensors of virtual micropolar strains and curvatures, respectively. The algebraic equilibrium equations of the finite element method will be thus obtained from the following fundamental integral principle

$$\int_V (\overline{\boldsymbol{\epsilon}} : \boldsymbol{\sigma} + \overline{\boldsymbol{\kappa}} : \boldsymbol{\mu}) dV - \int_V (\overline{\mathbf{w}} \cdot \mathbf{p}_{\mathrm{v}} + \overline{\boldsymbol{\varphi}} \cdot \mathbf{m}_{\mathrm{v}}) dV - \int_S (\overline{\mathbf{w}} \cdot \mathbf{p}_{\mathrm{s}} + \overline{\boldsymbol{\varphi}} \cdot \mathbf{m}_{\mathrm{s}}) dS = 0 \tag{13}$$

after an appropriate interpolation of the kinematic fields and their virtual counterparts has been specified. In the following section, we propose a generalisation of the standard Lagrangian interpolation, which includes the rotational degrees of freedom in the interpolation of the displacement vector - the so-called *linked interpolation* [33, 34, 28].

3. Governing equations of a 2D micropolar continuum.

In order to develop membrane finite elements, the presented boundary value problem is reduced from 3D to 2D. Consequently, the kinematic fields are in Cartesian coordinates reduced to only two independent displacements $\mathbf{w} = \langle u \; v \; 0 \rangle^{\mathrm{T}}$ and one microrotation $\boldsymbol{\varphi} = \langle 0 \; 0 \; \varphi \rangle^{\mathrm{T}}$, which represents an in-plane (or *drilling*) rotation. Furthermore, assuming a plane-strain condition, the stress and strain tensors are reduced to $\boldsymbol{\sigma} = \langle \sigma_{11} \;\; \sigma_{12} \;\; \sigma_{21} \;\; \sigma_{22} \rangle^{\mathrm{T}}$, $\boldsymbol{\mu} = \langle \mu_{31} \;\; \mu_{32} \rangle^{\mathrm{T}}$

and $\boldsymbol{\epsilon} = \langle \epsilon_{11} \;\; \epsilon_{12} \;\; \epsilon_{21} \;\; \epsilon_{22} \rangle^{\mathrm{T}}$, $\boldsymbol{\kappa} = \langle \kappa_{31} \;\; \kappa_{32} \rangle^{\mathrm{T}}$ respectively with

$$\begin{Bmatrix} \sigma_{11} \\ \sigma_{12} \\ \sigma_{21} \\ \sigma_{22} \end{Bmatrix} = \begin{bmatrix} (\lambda+2\mu) & 0 & 0 & \lambda \\ 0 & (\mu+\nu) & (\mu-\nu) & 0 \\ 0 & (\mu-\nu) & (\mu+\nu) & 0 \\ \lambda & 0 & 0 & (\lambda+2\mu) \end{bmatrix} \begin{Bmatrix} \epsilon_{11} \\ \epsilon_{12} \\ \epsilon_{21} \\ \epsilon_{22} \end{Bmatrix} \quad \Leftrightarrow \quad \boldsymbol{\sigma} = \mathbf{C_1}\boldsymbol{\epsilon}, \tag{14}$$

$$\begin{Bmatrix} \mu_{31} \\ \mu_{32} \end{Bmatrix} = \begin{bmatrix} (\beta+\gamma) & 0 \\ 0 & (\beta+\gamma) \end{bmatrix} \begin{Bmatrix} \kappa_{31} \\ \kappa_{32} \end{Bmatrix} \quad \Leftrightarrow \quad \boldsymbol{\mu} = \mathbf{C_2}\boldsymbol{\kappa}, \tag{15}$$

where $\mathbf{C_1}$ and $\mathbf{C_2}$ stand for the micropolar constitutive tensors. Therefore, the problem is reduced to only four elastic constants λ, μ, ν, and $\beta+\gamma$. The applied loading is likewise reduced to

$$\mathbf{p}_{\mathrm{v}} = \begin{Bmatrix} p_{v1} \\ p_{v2} \\ 0 \end{Bmatrix} = \begin{Bmatrix} \mathbf{q}_{\mathrm{v}} \\ 0 \end{Bmatrix}, \;\; \mathbf{m}_{\mathrm{v}} = \begin{Bmatrix} 0 \\ 0 \\ m_v \end{Bmatrix}, \tag{16}$$

$$\mathbf{p}_{\mathrm{s}} = \begin{Bmatrix} p_{s1} \\ p_{s2} \\ 0 \end{Bmatrix} = \begin{Bmatrix} \mathbf{q}_{\mathrm{s}} \\ 0 \end{Bmatrix}, \;\; \mathbf{m}_{\mathrm{s}} = \begin{Bmatrix} 0 \\ 0 \\ m_s \end{Bmatrix}. \tag{17}$$

185 The kinematic equations are reduced to

$$\underbrace{\begin{Bmatrix} \epsilon_{11} \\ \epsilon_{12} \\ \epsilon_{21} \\ \epsilon_{22} \end{Bmatrix}}_{\boldsymbol{\epsilon}} = \underbrace{\begin{bmatrix} \frac{\partial}{\partial x} & 0 \\ \frac{\partial}{\partial y} & 0 \\ 0 & \frac{\partial}{\partial x} \\ 0 & \frac{\partial}{\partial y} \end{bmatrix}}_{\mathbf{D_u}^{\mathrm{T}}} \underbrace{\begin{Bmatrix} u \\ v \end{Bmatrix}}_{\mathbf{u}} + \varphi \underbrace{\begin{Bmatrix} 0 \\ 1 \\ -1 \\ 0 \end{Bmatrix}}_{\mathbf{I}_\varphi} \quad \Leftrightarrow \quad \boldsymbol{\epsilon} = \mathbf{D_u}^{\mathrm{T}}\mathbf{u} + \varphi\mathbf{I}_\varphi, \tag{18}$$

while the curvatures are reduced to

$$\underbrace{\begin{Bmatrix} \kappa_{31} \\ \kappa_{32} \end{Bmatrix}}_{\boldsymbol{\kappa}} = \underbrace{\begin{Bmatrix} \frac{\partial}{\partial x} \\ \frac{\partial}{\partial y} \end{Bmatrix}}_{\mathbf{D_\mu}^{\mathrm{T}}} \varphi = \mathbf{D_\mu}^{\mathrm{T}}\varphi. \tag{19}$$

In order to obtain the numerical solution of the problem, the kinematic fields have to be approximated using a chosen type of interpolation. In general, the real and virtual kinematic fields are interpolated as $\mathbf{u}^h = \mathbf{N_u}\ \mathbf{d}^e$, $\varphi^h = \mathbf{N}_\varphi\ \mathbf{d}^e$, $\overline{\mathbf{u}}^h = \mathbf{N_u}\ \overline{\mathbf{d}}^e$, $\overline{\varphi}^h = \mathbf{N}_\varphi\ \overline{\mathbf{d}}^e$, where $\mathbf{N_u}$ and $\mathbf{N}_\varphi$ represent the matrices of interpolation functions over an element for the displacement and microrotation field, respectively, and $\mathbf{d}^e$ and $\overline{\mathbf{d}}^e$ represent the real and virtual vector of element nodal degrees of freedom, respectively. Superscript h denotes the discretization, while e denotes the element to which the interpolation is applied. After introducing the interpolation and substituting the kinematic and constitutive equations we obtain the interpolated element internal and external virtual works as

$$\begin{aligned} G^{int,e}(\mathbf{d}^e;\overline{\mathbf{d}}^e) = \ & \overline{\mathbf{d}}^{e\mathrm{T}} \int_V (\mathbf{N_u}^{\mathrm{T}}\mathbf{D_u} + \mathbf{N}_\varphi{}^{\mathrm{T}}\mathbf{I}_\varphi{}^{\mathrm{T}})\mathbf{C_1}(\mathbf{D_u}^{\mathrm{T}}\mathbf{N_u} + \mathbf{I}_\varphi\mathbf{N}_\varphi)dV\,\mathbf{d}^e + \\ & \overline{\mathbf{d}}^{e\mathrm{T}} \int_V (\mathbf{N}_\varphi{}^{\mathrm{T}}\mathbf{D}_{\boldsymbol{\varphi}})\mathbf{C_2}(\mathbf{D}_{\boldsymbol{\varphi}}{}^{\mathrm{T}}\mathbf{N}_\varphi)dV\,\mathbf{d}^e = \overline{\mathbf{d}}^{e\mathrm{T}}\mathbf{K}^e\mathbf{d}^e \end{aligned} \tag{20}$$

$$\begin{aligned} G^{ext,e}(\overline{\mathbf{d}}^e) = & \overline{\mathbf{d}}^{e\mathrm{T}} \int_V (\mathbf{N_u}^{\mathrm{T}}\mathbf{q}_{\mathrm{v}} + \mathbf{N}_\varphi{}^{\mathrm{T}}\mathbf{m}_{\mathrm{v}})dV + \overline{\mathbf{d}}^{e\mathrm{T}} \int_S (\mathbf{N_u}^{\mathrm{T}}\mathbf{q}_{\mathrm{s}} + \mathbf{N}_\varphi{}^{\mathrm{T}}\mathbf{m}_{\mathrm{s}})dS \\ = & \overline{\mathbf{d}}^{e\mathrm{T}}\mathbf{f}^e, \end{aligned} \tag{21}$$

where $\mathbf{K}^e$ and $\mathbf{f}^e$ represent the element stiffness matrix and external force vector.

The global internal and external virtual works are obtained as

$$G^{int}(\mathbf{d};\overline{\mathbf{d}}) = \mathop{\mathbb{A}}_{e=1}^{n_{elem}} G^{int,e}(\mathbf{d}^e;\overline{\mathbf{d}}^e) \equiv \overline{\mathbf{d}}^{\mathrm{T}}\mathbf{K}\mathbf{d}, \quad G^{ext}(\overline{\mathbf{d}}) = \mathop{\mathbb{A}}_{e=1}^{n_{elem}} G^{ext,e}(\overline{\mathbf{d}}^e) \equiv \overline{\mathbf{d}}^{\mathrm{T}}\mathbf{f} \tag{22}$$

with $\mathbf{d}$ and $\overline{\mathbf{d}}$ as the global vectors of real and virtual displacements, $\mathbf{K} = \mathop{\mathbb{A}}_{e=1}^{n_{elem}} \mathbf{K}^e$ and $\mathbf{f} = \mathop{\mathbb{A}}_{e=1}^{n_{elem}} \mathbf{f}^e$ as the global stifness matrix and external force vector, n_{elem} as the total number of elements in the mesh, and $\mathbb{A}$ as the finite-element assembly operator [35]. Finally, by substituting G^{int} and G^{ext} in (11) we obtain the approximated weak form. Recognising arbitrariness of $\overline{\mathbf{d}}$, we eventually obtain the basic set of algebraic equations of the finite element method as $\mathbf{K}\,\mathbf{d} = \mathbf{f}$.

4. Lagrangian and linked interpolation

Within this paper two different interpolations are compared for the families of triangular and quadrilateral finite elements. The first one is the conventional Lagrange interpolation [36], serving to approximate the real and virtual displacements as

$$\mathbf{u}^h = \mathbf{N}_u \mathbf{d}^e, \quad \overline{\mathbf{u}}^h = \mathbf{N}_u \overline{\mathbf{d}}^e, \tag{23}$$

and the real and virtual microrotation as

$$\varphi^h = \mathbf{N}_\varphi \ \mathbf{d}^e, \quad \overline{\varphi}^h = \mathbf{N}_\varphi \ \overline{\mathbf{d}}^e, \tag{24}$$

with

$$\mathbf{N}_u = \begin{bmatrix} N_1 & 0 & 0 & \dots & N_{n_{node}} & 0 & 0 \\ 0 & N_1 & 0 & \dots & 0 & N_{n_{node}} & 0 \end{bmatrix} \quad \text{and} \tag{25}$$

$$\mathbf{N}_\varphi = \langle 0 \quad 0 \quad N_1 \quad \dots \quad 0 \quad 0 \quad N_{n_{node}} \rangle, \tag{26}$$

n_{node} as the number of nodes on the element and $N_i (i = 1, ..., n_{node})$ as the i^{th} Lagrangian polynomial. The second interpolation analysed is the linked interpolation in which the displacement field depends on the nodal microrotation, too. The linked interpolation for the displacement field consists of the conventional Lagrange interpolation (represented by matrix $\mathbf{N}_u$) enhanced by the contribution due to the nodal microrotations. In general, the linked interpolation is therefore given as

$$\mathbf{u}^h = (\mathbf{N}_u + \mathbf{N}_{enh})\mathbf{d}^e, \quad \overline{\mathbf{u}}^h = (\mathbf{N}_u + \mathbf{N}_{enh})\overline{\mathbf{d}}^e, \tag{27}$$

where $\mathbf{N}_{enh}$ is the matrix of linked-interpolation enhancement to the Lagrangian interpolation. In the linked-interpolation framework, the microrotations are still interpolated conventionally, as defined in equation (24).

The linked interpolation is in [28] derived as the exact solution of differential equations of a 3D Timoshenko beam. For the present purposes let us limit our

attention to its 2D form [29, 30], where the displacement field along the in-plane axis z orthogonal to the centroidal line x of the beam is

$$w = \sum_{i=1}^{n_{node}} N_i w_i - \frac{L}{n_{node}} \sum_{i=1}^{n_{node}} \frac{\xi - \xi_i}{2} N_i \varphi_i, \tag{28}$$

while the rotation field around the out-of-plane axis y orthogonal to the centroidal line is simply

$$\varphi = \sum_{i=1}^{n_{node}} N_i \varphi_i, \tag{29}$$

where L is the finite-element length, $\xi \in [-1, 1]$ is the natural co-ordinate, n_{node} is the number of nodes on the element, φ_i and w_i are the rotation and the displacement at the i^{th} node, N_i is the i^{th} Lagrange polynomial of order $n_{node}-1$, ξ_i is the natural co-ordinate of the i^{th} node, and the axes x, y, z form a right-handed co-ordinate system. The displacement field is thus interpolated by a polynomial one order higher than that used for the rotations. The Lagrangian polynomials are given as

$$N_i = \prod_{\substack{j=1 \\ j \neq i}}^{n_{node}} \frac{(\xi_j - \xi)}{(\xi_j - \xi_i)}, \qquad i = 1, ..., n_{node}. \tag{30}$$

In order to generalise the linked interpolation concept presented to 2D micropolar continuum, it is important to note that, in contrast to beams, for this continuum in general there does not exist a closed-form solution of the differential equations. The approach that we take is the following: (i) we apply interpolation (28) *to the element edges only*, i.e. we treat the element edges as beam finite elements and (ii) we average the edge results within the interior of the element depending on the actual position, so that that interpolation correctly describes rigid-body motion. To do this, we follow the approach proposed in [29, 30] for the Mindlin plate elements.

4.1. Triangular finite elements

The triangular finite element family with the related shape functions is defined in the natural coordinate system. The mapping from the natural coordi-

nate system (ξ, η) to the Cartesian coordinate system (x, y) is defined as:

$$x = \sum_{a=1}^{n_{node}} N_a(\xi, \eta) x_a, \quad y = \sum_{a=1}^{n_{node}} N_a(\xi, \eta) y_a, \tag{31}$$

where n_{node} stands for the number of element nodes, (x_a, y_a) represent the element nodal coordinates in the Cartesian coordinate system and $N_a(\xi, \eta)$ represent the isoparametric shape functions with arguments ξ, η which run between $[0, 1]$. Here we consider the elements with three, six or ten nodes, with a node-numbering convention as shown in Figure 1.

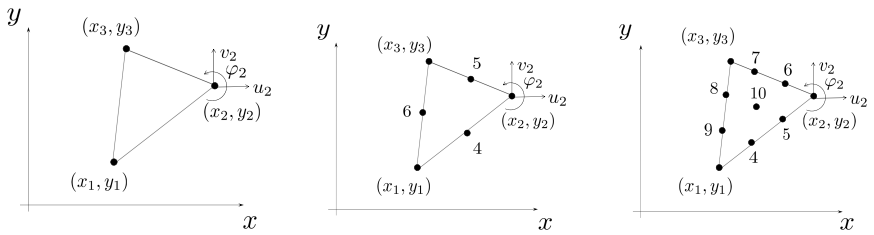

(a) Order 1 element (T3) (b) Order 2 element (T6) (c) Order 3 element (T10)

Figure 1: Triangular finite elements of different order

The shape functions in (31) are most easily expressed via a set of the so-called area coordinates

$$\zeta_1(\xi, \eta) = 1 - \xi - \eta, \quad \zeta_2(\xi, \eta) = \xi, \quad \zeta_3(\xi, \eta) = \eta. \tag{32}$$

For the edge nodes in Figure 1 taken at the edge halves in T6 and at the edge thirds in T10 and the inner node in T10 in its centroid they are given in Table 1.

Table 1: Triangular shape functions

Element	T3	T6	T10
Vertex shape functions $(a = 1, 2, 3)$	$N_a = \zeta_a$	$N_a = \zeta_a(2\zeta_a - 1)$	$N_a = \frac{1}{2}\zeta_a(3\zeta_a - 1)(3\zeta_a - 2)$
Edge shape functions $(i = 1, 2, 3,$ $j = \max(1; i + 1 < 4))$	-	$N_{i+3} = 4\zeta_i\zeta_j$	$N_{2i+2} = \frac{9}{2}\zeta_i\zeta_j(3\zeta_i - 1)$ $N_{2i+3} = \frac{9}{2}\zeta_i\zeta_j(3\zeta_j - 1)$
Centroid node shape function	-	-	$N_{10} = 27\zeta_1\zeta_2\zeta_3$

For the Lagrangian family of elements the same shape functions are used for the interpolation of real and virtual displacements and rotations as given in equations (23) and (24). For the family of elements with linked interpolation, the rotations are still interpolated using the Lagrange polynomials and (24), but in the displacement field we now have an enhancement in the displacement field as shown in equation (27). For the elements of different order, this enhancement is now defined following the approach given in [30].

Triangular membrane element with three nodes (T3 + LI). In analogy with the linked interpolation for a beam element (28), when applied to a two-noded beam, we propose the linked interpolation for the triangular element with three nodes and three degrees of freedom per node, named T3 + LI and shown in Figure 1a) such that

$$\begin{aligned}\mathbf{u}^h = (\mathbf{N}_u + \mathbf{N}_{enh})\mathbf{d}^e &= \sum_{a=1}^{3} N_a \mathbf{u}_a + \frac{1}{2}\zeta_2\zeta_3(\varphi_2 - \varphi_3)\begin{Bmatrix} y_2 - y_3 \\ x_3 - x_2 \end{Bmatrix} + \\ &+ \frac{1}{2}\zeta_3\zeta_1(\varphi_3 - \varphi_1)\begin{Bmatrix} y_3 - y_1 \\ x_1 - x_3 \end{Bmatrix} + \\ &+ \frac{1}{2}\zeta_1\zeta_2(\varphi_1 - \varphi_2)\begin{Bmatrix} y_1 - y_2 \\ x_2 - x_1 \end{Bmatrix} \\ &= \sum_{a=1}^{3} N_a \mathbf{u}_a + \begin{Bmatrix} f_{1,x} \\ f_{1,y} \end{Bmatrix}(\varphi_2 - \varphi_3) + \begin{Bmatrix} f_{2,x} \\ f_{2,y} \end{Bmatrix}(\varphi_3 - \varphi_1) + \\ &+ \begin{Bmatrix} f_{3,x} \\ f_{3,y} \end{Bmatrix}(\varphi_1 - \varphi_2) \end{aligned} \tag{33}$$

where $f_{i,x} = \frac{1}{2}\zeta_j\zeta_k(y_j - y_k)$, $f_{i,y} = \frac{1}{2}\zeta_j\zeta_k(x_k - x_j)$ and i, j, k is a cyclic permutation of $1, 2, 3$ resulting in $\mathbf{N}_{enh} = \begin{bmatrix}\mathbf{N}_{enh,1} & \mathbf{N}_{enh,2} & \mathbf{N}_{enh,3}\end{bmatrix}$ where

$$\mathbf{N}_{enh,i} = \begin{bmatrix} 0 & 0 & f_{k,x} - f_{j,x} \\ 0 & 0 & f_{k,y} - f_{j,y} \end{bmatrix}. \tag{34}$$

Triangular membrane element with six nodes (T6 + LI). Now we generalise the linked interpolation of a beam element (28) applied to a three-noded beam to a triangular element with six nodes and three degrees of freedom per node, named T6 + LI and shown in Figure 1b). The displacement interpolation thus follows as

$$\mathbf{u}^h = (\mathbf{N}_u + \mathbf{N}_{enh})\mathbf{d}^e = \sum_{a=1}^{6} N_a(\xi,\eta) \begin{Bmatrix} u_a \\ v_a \end{Bmatrix} + \\ + \frac{1}{3}\zeta_1\zeta_2(\zeta_2-\zeta_1)(\varphi_1 - 2\varphi_4 + \varphi_2) \begin{Bmatrix} y_2 - y_1 \\ x_1 - x_2 \end{Bmatrix} + \\ + \frac{1}{3}\zeta_2\zeta_3(\zeta_3-\zeta_2)(\varphi_2 - 2\varphi_5 + \varphi_3) \begin{Bmatrix} y_3 - y_2 \\ x_2 - x_3 \end{Bmatrix} + \\ + \frac{1}{3}\zeta_3\zeta_1(\zeta_1-\zeta_3)(\varphi_3 - 2\varphi_6 + \varphi_1) \begin{Bmatrix} y_1 - y_3 \\ x_3 - x_1 \end{Bmatrix} \tag{35}$$

from where $\mathbf{N}_{enh}$ immediately follows.

Triangular membrane element with ten nodes (T10 + LI). Finally, we develop the triangular element with ten nodes shown in Figure 1c), which we name T10 + LI. Generalising the linked interpolation for a beam element (28) applied to a four-node element

$$\mathbf{u}^h = (\mathbf{N}_u + \mathbf{N}_{enh})\mathbf{d}^e = \sum_{a=1}^{10} N_a(\xi,\eta) \begin{Bmatrix} u_a \\ v_a \end{Bmatrix} + \\ + \frac{1}{8}\zeta_1\zeta_2(3\zeta_1-1)(3\zeta_2-1) \begin{Bmatrix} y_2 - y_1 \\ x_1 - x_2 \end{Bmatrix} (\varphi_1 - 3\varphi_4 + 3\varphi_5 - \varphi_2) + \\ + \frac{1}{8}\zeta_2\zeta_3(3\zeta_2-1)(3\zeta_3-1) \begin{Bmatrix} y_3 - y_2 \\ x_2 - x_3 \end{Bmatrix} (\varphi_2 - 3\varphi_6 + 3\varphi_7 - \varphi_3) + \\ + \frac{1}{8}\zeta_3\zeta_1(3\zeta_3-1)(3\zeta_1-1) \begin{Bmatrix} y_1 - y_3 \\ x_3 - x_1 \end{Bmatrix} (\varphi_3 - 3\varphi_8 + 3\varphi_9 - \varphi_1), \tag{36}$$

from where $\mathbf{N}_{enh}$ again immediately follows.

4.2. Quadrilateral finite elements

The second family of finite elements we develop are quadrilateral elements of order 1, 2 and 3 shown in Figure 2 with three degrees of freedom per node

(horizontal and vertical displacements, microrotation). As for the triangular elements, the quadrilateral finite element family and the corresponding shape functions are defined in the natural coordinate system where the mapping is again defined by (31), where here we consider the elements with four, nine and sixteen nodes (Q4, Q9, Q16) and ξ and η run between $[-1, 1]$. The node-numbering convention for the elements is shown in Figure 2.

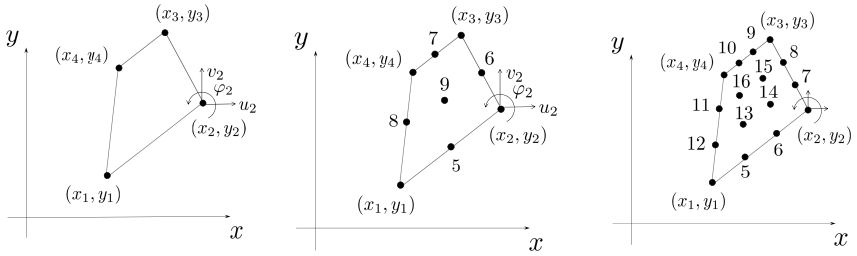

(a) Order 1 element (Q4) (b) Order 2 element (Q9) (c) Order 3 element (Q16)

Figure 2: Quadrilateral finite elements of different order

The shape functions in (31) are given for $\xi_1 = \xi_4 = -1,\ \xi_2 = \xi_3 = +1,\ \eta_1 = \eta_2 = -1,\ \eta_3 = \eta_4 = +1$ as follows. For Q4, they are defined as $N_a(\xi, \eta) = \frac{1}{4}(1 + \xi_a\xi)(1 + \eta_a\eta)$. For Q9 with $\xi_8 = -1,\ \xi_5 = \xi_7 = \xi_9 = 0,\ \xi_6 = +1,\ \eta_5 = -1,\ \eta_6 = \eta_8 = \eta_9 = 0$ and $\eta_7 = +1$ they are given as

$$\begin{aligned}
&\text{Vertex nodes:} && N_a = \frac{1}{4}\xi\eta(\xi + \xi_a)(\eta + \eta_a),\\
&\text{Edge nodes 5 and 7:} && N_a = \frac{1}{2}\eta(1 - \xi^2)(\eta + \eta_a),\\
&\text{Edge nodes 6 and 8:} && N_a = \frac{1}{2}\xi(\xi + \xi_a)(1 - \eta^2),\\
&\text{Central node:} && N_9 = (1 - \xi^2)(1 - \eta^2).
\end{aligned}$$

while for Q16 with $\xi_{11} = \xi_{12} = -1,\ \xi_5 = \xi_{10} = \xi_{13} = \xi_{16} = -\frac{1}{3},\ \xi_6 = \xi_9 = \xi_{14} = \xi_{15} = +\frac{1}{3},\ \xi_7 = \xi_8 = +1,\ \eta_5 = \eta_6 = -1,\ \eta_7 = \eta_{12} = \eta_{13} = \eta_{14} = -\frac{1}{3},$

$\eta_8 = \eta_{11} = \eta_{15} = \eta_{16} = +\frac{1}{3}$ and $\eta_9 = \eta_{10} = +1$ they are given as

$$\begin{aligned}
&\text{Vertex nodes:} && N_a = \frac{81}{256}(1+\xi_a\xi)(1+\eta_a\eta)(\frac{1}{9}-\xi^2)(\frac{1}{9}-\eta^2),\\
&\text{Edge nodes with } \xi_a = \pm 1 \text{ and } \eta_a = \pm\frac{1}{3}: && N_a = \frac{243}{256}(1-\xi^2)(\eta^2-\frac{1}{9})(\frac{1}{3}+3\xi_a\xi)(1+\eta_a\eta),\\
&\text{Edge nodes with } \xi_a = \pm\frac{1}{3} \text{ and } \eta_a = \pm 1: && N_a = \frac{243}{256}(1-\eta^2)(\xi^2-\frac{1}{9})(\frac{1}{3}+3\eta_a\eta)(1+\xi_a\xi),\\
&\text{Internal nodes:} && N_a = \frac{729}{256}(1-\xi^2)(1-\eta^2)(\frac{1}{3}+3\eta_a\eta)(\frac{1}{3}+3\xi_a\xi).
\end{aligned}$$

As in the family of triangular elements, for the quadrilateral elements of the Lagrangian type, the interpolation for the displacements and rotations are given by (23) and (24), the latter again also remaining valid for the quadrilateral family of elements with linked interpolation. The enhancement in the displacement field $\mathbf{N}_{enh}$ in (27) is now defined following the approach given in [29], based on the expression (28) for the linked interpolation in beams.

In [29] the authors have additionally enhanced the proposed finite elements with linked interpolation by introducing additional bubble modes. However, their numerical results have shown that the bubble mode contribution to the obtained result is negligible, except for the higher order patch test satisfaction. Therefore, the presented elements are not enhanced with additional modes.

Quadrilateral finite element with four nodes (Q4 + LI). For the quadrilateral element with four nodes shown in Figure 2a), named Q4 + LI, we define the

displacement interpolation as

$$\begin{aligned}
\mathbf{u}^h = (\mathbf{N}_u + \mathbf{N}_{enh})\mathbf{d}^e = &\sum_{a=1}^{4} N_a(\xi,\eta)\begin{Bmatrix} u_a \\ v_a \end{Bmatrix} + \\
&+ \frac{1}{8}\frac{1}{2}(1-\xi^2)(1-\eta)\begin{Bmatrix} y_2 - y_1 \\ x_1 - x_2 \end{Bmatrix}(\varphi_2 - \varphi_1) + \\
&+ \frac{1}{8}\frac{1}{2}(1+\xi)(1-\eta^2)\begin{Bmatrix} y_3 - y_2 \\ x_2 - x_3 \end{Bmatrix}(\varphi_3 - \varphi_2) + \\
&+ \frac{1}{8}\frac{1}{2}(1-\xi^2)(1+\eta)\begin{Bmatrix} y_4 - y_3 \\ x_3 - x_4 \end{Bmatrix}(\varphi_4 - \varphi_3) + \\
&+ \frac{1}{8}\frac{1}{2}(1-\xi)(1-\eta^2)\begin{Bmatrix} y_1 - y_4 \\ x_4 - x_1 \end{Bmatrix}(\varphi_1 - \varphi_4) \\
= &\sum_{a=1}^{4} N_a(\xi,\eta)\begin{Bmatrix} u_a \\ v_a \end{Bmatrix} + \\
&+ \begin{Bmatrix} f_{1,x} \\ f_{1,y} \end{Bmatrix}(\varphi_2 - \varphi_3) + \begin{Bmatrix} f_{2,x} \\ f_{2,y} \end{Bmatrix}(\varphi_3 - \varphi_4) + \\
&+ \begin{Bmatrix} f_{3,x} \\ f_{3,y} \end{Bmatrix}(\varphi_4 - \varphi_1) + \begin{Bmatrix} f_{4,x} \\ f_{4,y} \end{Bmatrix}(\varphi_1 - \varphi_2), \qquad (37)
\end{aligned}$$

where $f_{1,x} = \frac{1}{16}(1+\xi)(1-\eta^2)(y_2 - y_3)$, $f_{2,x} = \frac{1}{16}(1-\xi^2)(1+\eta)(y_3 - y_4)$, $f_{3,x} = \frac{1}{16}(1-\xi)(1-\eta^2)(y_4 - y_1)$, $f_{4,x} = \frac{1}{16}(1-\xi^2)(1-\eta)(y_1 - y_2)$ and $f_{1,y} = \frac{1}{16}(1+\xi)(1-\eta^2)(x_3 - x_2)$, $f_{2,y} = \frac{1}{16}(1-\xi^2)(1+\eta)(x_4 - x_3)$, $f_{3,y} = \frac{1}{16}(1-\xi)(1-\eta^2)(x_1 - x_4)$, $f_{4,y} = \frac{1}{16}(1-\xi^2)(1-\eta)(x_2 - x_1)$ resulting in $\mathbf{N}_{enh} = \begin{bmatrix}\mathbf{N}_{enh,1} & \mathbf{N}_{enh,2} & \mathbf{N}_{enh,3} & \mathbf{N}_{enh,4}\end{bmatrix}$ where

$$\begin{aligned}
\mathbf{N}_{enh,1} &= \begin{bmatrix} 0 & 0 & f_{4,x} - f_{3,x} \\ 0 & 0 & f_{4,y} - f_{3,y} \end{bmatrix}, \quad \mathbf{N}_{enh,2} = \begin{bmatrix} 0 & 0 & f_{1,x} - f_{4,x} \\ 0 & 0 & f_{1,y} - f_{4,y} \end{bmatrix}, \qquad (38) \\
\mathbf{N}_{enh,3} &= \begin{bmatrix} 0 & 0 & f_{2,x} - f_{1,x} \\ 0 & 0 & f_{2,y} - f_{1,y} \end{bmatrix}, \quad \mathbf{N}_{enh,4} = \begin{bmatrix} 0 & 0 & f_{3,x} - f_{2,x} \\ 0 & 0 & f_{3,y} - f_{2,y} \end{bmatrix}.
\end{aligned}$$

Quadrilateral finite element with nine nodes (Q9+LI). For the quadrilateral element with nine nodes shown in Figure 2b), named Q9 + LI, we define the

displacement interpolation as

$$
\begin{aligned}
\mathbf{u}^h =& (\mathbf{N}_u + \mathbf{N}_{enh})\mathbf{d}^e = \sum_{a=1}^{9} N_a(\xi,\eta) \begin{Bmatrix} u_a \\ v_a \end{Bmatrix} + \\
& - \frac{1}{8}\frac{1}{3}\xi\eta(1-\xi^2)(1-\eta) \begin{Bmatrix} y_2 - y_1 \\ x_1 - x_2 \end{Bmatrix} (\varphi_1 - 2\varphi_5 + \varphi_2) + \\
& + \frac{1}{4}\frac{1}{3}\xi(1-\xi^2)(1-\eta^2) \begin{Bmatrix} y_6 - y_8 \\ x_8 - x_6 \end{Bmatrix} (\varphi_8 - 2\varphi_9 + \varphi_6) + \\
& + \frac{1}{8}\frac{1}{3}\xi\eta(1-\xi^2)(1+\eta) \begin{Bmatrix} y_3 - y_4 \\ x_4 - x_3 \end{Bmatrix} (\varphi_4 - 2\varphi_7 + \varphi_3) + \\
& + \frac{1}{8}\frac{1}{3}\xi\eta(1-\xi)(1-\eta^2) \begin{Bmatrix} y_4 - y_1 \\ x_1 - x_4 \end{Bmatrix} (\varphi_1 - 2\varphi_8 + \varphi_4) + \\
& - \frac{1}{4}\frac{1}{3}\eta(1-\xi^2)(1-\eta^2) \begin{Bmatrix} y_7 - y_5 \\ x_5 - x_7 \end{Bmatrix} (\varphi_5 - 2\varphi_9 + \varphi_7) + \\
& - \frac{1}{8}\frac{1}{3}\xi\eta(1+\xi)(1-\eta^2) \begin{Bmatrix} y_3 - y_2 \\ x_2 - x_3 \end{Bmatrix} (\varphi_2 - 2\varphi_6 + \varphi_3)
\end{aligned}
\tag{39}
$$

from where $\mathbf{N}_{enh}$ follows in a straight-forward way.

Quadrilateral finite element with sixteen nodes (Q16+LI). For the quadrilateral element with sixteen nodes shown in Figure 2c) and named Q16 + LI, we define

the displacement interpolation as

$$
\begin{aligned}
\mathbf{u}^h =&(\mathbf{N}_u + \mathbf{N}_{enh})\mathbf{d}^e = \sum_{a=1}^{16} N_a(\xi,\eta) \begin{Bmatrix} u_a \\ v_a \end{Bmatrix} + \\
&+ \frac{1}{4} I_{1\eta} N_\xi \begin{Bmatrix} y_2 - y_1 \\ x_1 - x_2 \end{Bmatrix} (\varphi_1 - 3\varphi_5 + 3\varphi_6 - \varphi_2) + \\
&+ \frac{1}{4} I_{2\eta} N_\xi \begin{Bmatrix} y_7 - y_{12} \\ x_{12} - x_7 \end{Bmatrix} (\varphi_{12} - 3\varphi_{13} + 3\varphi_{14} - \varphi_7) + \\
&+ \frac{1}{4} I_{3\eta} N_\xi \begin{Bmatrix} y_8 - y_{11} \\ x_{11} - x_8 \end{Bmatrix} (\varphi_{11} - 3\varphi_{16} + 3\varphi_{15} - \varphi_8) + \\
&+ \frac{1}{4} I_{4\eta} N_\xi \begin{Bmatrix} y_3 - y_4 \\ x_4 - x_3 \end{Bmatrix} (\varphi_4 - 3\varphi_{10} + 3\varphi_9 - \varphi_3) + \\
&- \frac{1}{4} I_{1\xi} N_\eta \begin{Bmatrix} y_4 - y_1 \\ x_1 - x_4 \end{Bmatrix} (\varphi_1 - 3\varphi_{12} + 3\varphi_{11} - \varphi_4) + \\
&- \frac{1}{4} I_{2\xi} N_\eta \begin{Bmatrix} y_{10} - y_5 \\ x_5 - x_{10} \end{Bmatrix} (\varphi_5 - 3\varphi_{13} + 3\varphi_{16} - \varphi_{10}) + \\
&- \frac{1}{4} I_{3\xi} N_\eta \begin{Bmatrix} y_9 - y_6 \\ x_6 - x_9 \end{Bmatrix} (\varphi_6 - 3\varphi_{14} + 3\varphi_{15} - \varphi_9) + \\
&- \frac{1}{4} I_{4\xi} N_\eta \begin{Bmatrix} y_3 - y_2 \\ x_2 - x_3 \end{Bmatrix} (\varphi_2 - 3\varphi_7 + 3\varphi_8 - \varphi_3)
\end{aligned} \tag{40}
$$

where $I_{1\xi} = -\frac{9}{16}(\xi^2 - \frac{1}{9})(\xi - 1)$, $I_{2\xi} = \frac{27}{16}(\xi^2 - 1)(\xi - \frac{1}{3})$, $I_{3\xi} = \frac{27}{16}(\xi^2 - 1)(\xi + \frac{1}{3})$, $I_{4\xi} = \frac{9}{16}(\xi^2 - \frac{1}{9})(\xi + 1)$, $N_\xi = \frac{9}{32}(\xi^2 - \frac{1}{9})(\xi^2 - 1)$,and analogously for $I_{1\eta}$, $I_{2\eta}$, $I_{3\eta}$, $I_{4\eta}, N_\eta$ using the variable η. From here, $\mathbf{N}_{enh}$ again follows immediately.

5. Numerical examples

In this section the presented families of elements are analysed through four numerical examples. The convergence analysis is performed on a force patch test using a regular mesh in Section 5.1 and the conclusions drawn are implemented

in the procedure to run the displacement patch test on an irregular mesh (Section 5.2) due to Providas [37]. In Section 5.3, an infinite plate with a cylindrical hole subject to uniform tension is analysed and the results are compared to the analytical solution [6]. Finally, in Section 5.4, a cantilever beam in pure bending is analysed against the analytical solution [15]. In all the examples, both the standard Lagrange finite elements and the newly presented linked-interpolation finite elements are tested.

5.1. Force patch test: cantilever beam subject to pure tension

A force patch test shown in Figure 3 is performed on a cantilever beam of length $L = 10$ m, height $h = 2$ m and a unit thickness subject to pure axial distributed loading $p = 10\ \mathrm{N/m^2}$ using a number of regular meshes. The micropolar material parameters used are equal to $\mu = 1000\ \ \mathrm{N/m^2}$, $\lambda = 1000\ \mathrm{N/m^2}$, $\nu = 500\ \mathrm{N/m^2}$ and $\beta = \gamma = 20$ N.

In this example the analytical results for the stress fields (all components of the stress tensor and the couple-stress tensor equal to zero apart from the axial tension, which is equal to p) and the axial displacement at the free end (pL/E) are expected be obtained for an arbitrary number of finite elements in the mesh. The results of the test for triangular and quadrilateral finite elements with the conventional (Lagrange) interpolation and with the newly proposed linked interpolation are given in Table 2.

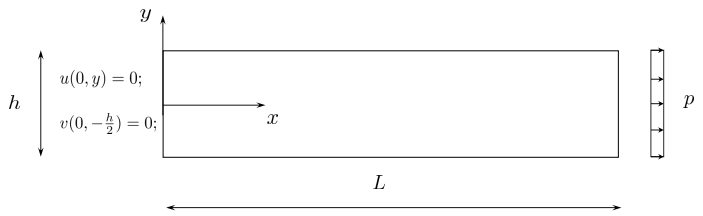

Figure 3: A cantilever beam subject to pure tension

To understand why most of the linked-interpolation elements fail this test and find the solution for how to modify them in order to pass it, an inversely

posed problem has been studied: the correct nodal displacement and rotations have been prescribed to the elements with linked interpolation and the resulting stress and couple-stress tensors as well as the nodal load vector have been analysed. It turns out that the all the stress and stress-couple components are exact but, in the nodal load vector, the incorrect moment components are generated by the linked interpolation applied to the virtual displacements. Interstingly, this does not happen in the quadratic elements T6+LI and Q9+LI.

Table 2: Results for the force patch test

Triangular elements		Quadrilateral elements	
Element	RESULT	Element	RESULT
T3	passed	Q4	passed
T3+LI	failed	Q4+LI	failed
T6	passed	Q9	passed
T6+LI	passed	Q9+LI	passed
T10	passed	Q16	passed
T10+LI	failed	Q16+LI	failed

Motivated by this observation, a solution is found by applying the *Petrov–Galerkin* finite-element method, which is based on *different interpolation* for the test and the trail functions – here the virtual and the actual displacement fields. To eliminate the anomalous nodal moments caused by the linked interpolation of the virtual displacements $\overline{\mathbf{u}}$, here we choose to *interpolate them using the standard Lagrangian polynomials*, i.e.

$$\overline{\mathbf{u}} = \mathbf{N}_u \overline{\mathbf{d}}, \tag{41}$$

The real displacements, however, are still interpolated using the linked interpo-

lation, i.e.

$$\mathbf{u} = (\mathbf{N}_u + \mathbf{N}_{enh})\mathbf{d}, \tag{42}$$

The microrotation interpolation remains unchanged in both its virtual and its real form, i.e. $\overline{\varphi} = \mathbf{N}_\varphi \overline{\mathbf{d}}$ and $\varphi = \mathbf{N}_\varphi \mathbf{d}$. The Petrov-Galerkin modification described is applied to those elements which fail the patch test. We refer to these elements as T3+LI (PG), T10+LI (PG), Q4+LI (PG) and Q10+LI (PG). When performing the same patch test using the elements based on the Petrov-Galerkin method, the patch test for all the elements is passed.

To understand why the quadratic elements with linked interpolation (T6+LI and Q9+LI) pass this patch test, while the linear and the cubic elements (T3+LI, T10+LI, Q4+LI and Q16+LI) do not, let us pinpoint the main difference between these two groups of elements in the character of the enhanced shape functions caused by the linked interpolation. In the linear and the cubic elements, the enhancement is symmetric, which, when integrated over the element domain, give a non-zero value, and thus provide non-desired nodal moments for the constant-stress state present here. On the other hand, the enhanced interpolation functions for the quadratic elements are antisymmetric and thus integrate to zero for the constant-stress state. Clearly, for quadrilaterals, this argument is applicable only to rectangular quadratic elements. For non-regular meshes, Q9+LI should not be expected to retain this property and would have to be accordingly modified into Q9+LI (PG).

Another approach to satisfy the convergence criteria may be provided along the lines of the modification of the matrix of enhanced interpolation proposed by Wilson and Ibrahimbegović [38]. In their work they impose the requirement that the enhanced part of the interpolation under the state of constant stress does not contribute to the strain energy. In order to satisfy this requirement, the matrix of enhanced interpolation has to be modified by adding a constant correction matrix, which makes the enhanced part to vanish for a state of constant stress. Even though in this work this approach is not analysed, we point out that it is

a possible methodology for modifying the elements with linked interpolation to satisfy the patch test. A detailed explanation of this approach is provided in [38].

5.2. Displacement patch tests for the micropolar continuum

According to Providas [37] the patch test for micropolar finite elements should consist of a set of three separate tests. The tests are performed on a rectangular domain bounded by the sides connecting the points 1–4 in Figure 4 and discretised using the distorted finite-element mesh shown. The length and height of the domain are $L = 0.24$ m, $H = 0.12$ m and the coordinates of the internal nodes 5–8 are the following 5=(0.04,0.02), 6=(0.18,0.03), 7=(0.08,0.08) and 8=(0.16,0.08). The material parameters used are the same as defined in the force patch test example. The displacements and microrotations are imposed on the external nodes, while the volume loading (if any) is imposed on the interior of the domain. The element passes a patch test if the internal nodes are capable of reproducing the analytical solution imposed by the boundary conditions.

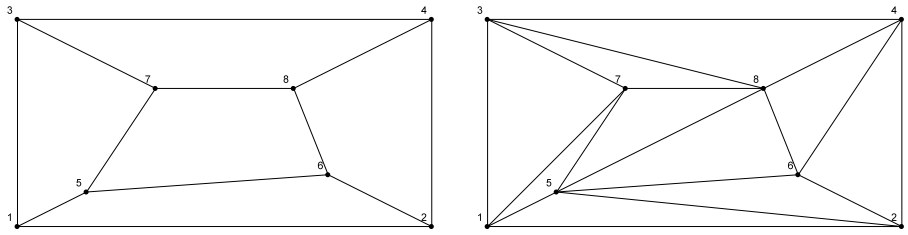

(a) Displacement patch test: quadrilateral FE mesh

(b) Displacement patch test: triangular FE mesh

Figure 4: Finite element mesh for the displacement patch test

The first test is the standard patch test of the finite elements in the classical continuum theory, whereby imposing linearly varying displacement and a constant microrotation field via appropriate boundary conditions we obtain the state of *constant symmetric stress and strain*. The fields are defined as follows:

$$u = 10^{-3}(x + 0.5y), \quad v = 10^{-3}(x + y), \quad \varphi = 0.25 \cdot 10^{-3}. \tag{43}$$

The second test describes the state of *constant non-symmetric shear* (both in stress and strain), for which a constant body moment is needed. The actual input is given as

$$u = 10^{-3}(x + 0.5y), \quad v = 10^{-3}(x + y), \quad \varphi = 0.75 \cdot 10^{-3}, \quad m_v = 1. \tag{44}$$

The third test describes the state of constant curvature, whereby imposing linearly varying displacement, microrotation and body moment fields as well as a constant body force field we obtain linearly varying stresses and *constant couple-stresses*. Providas considers the third patch test to be a necessary condition for finite-element convergence even though in this test the shear stresses are *linearly varying*:

$$\begin{gathered} u = 10^{-3}(x + 0.5y), \quad v = 10^{-3}(x + y), \quad \varphi = 10^{-3}(0.25 + (x - y)), \\ p_x = p_y = 1, \quad m_v = 2(x - y). \end{gathered} \tag{45}$$

According to [36], however, satisfaction of a patch test in which stress distribution is variable is not necessary for convergence and, for this reason, we consider this test to be a *higher-order patch test*, analogous to a pure bending test.

The constant stress tests are analysed first. As indicated earlier, when using an irregular mesh present here, the Q9+LI element fails the first two patch tests. Its Petrov-Galerkin modification Q9+LI (PG), however, passes them, as do also all the other proposed elements.

Regarding the third test, all the elements in which the standard Lagrangian interpolation has been utilised pass it (as does also the element given in [39]), which is expected even though it contradicts the results in the literature [37, 40]. For the highest-order elements T10 and Q16, however, the amount of data provided on the boundary has not been sufficient and four additional internal nodes have had to be additionally prescribed the field values to pass it. Concerning the family of elements with linked interpolation, T3+LI (PG) and Q4+LI (PG) fail to pass this test, while all the higher-order elements pass it. The results of

the third test for the elements which do not pass it are presented in Table 3. Even though this patch test is not satisfied for the lower-order elements of finite size, we consider that all the proposed elements satisfy the convergence criteria since, as argued earlier, they are able to reproduce exactly any state of constant stress.

Table 3: Results for Patch test 3 [37]

(a) Displacements at node 6 and stresses in Gauss point at (0.0933, 0.006667)

Element	$u \times 10^{-3}$	$v \times 10^{-3}$	$\varphi \times 10^{-3}$	σ_{11}	σ_{12}	σ_{21}	μ_{31}	μ_{32}
T3	0.195	0.210	0.400	4.00	1.59	1.41	0.04	-0.040
T3+LI (PG)	0.194	0.205	0.401	4.01	1.54	1.36	0.04	-0.041
Exact	0.195	0.210	0.400	4.00	1.59	1.41	0.04	-0.040

(b) Displacements at node 6 and stresses in Gauss point at (0.176027, 0.0281456)

Element	$u \times 10^{-3}$	$v \times 10^{-3}$	$\varphi \times 10^{-3}$	σ_{11}	σ_{12}	σ_{21}	μ_{31}	μ_{32}
Q4	0.1950	0.210	0.400	4.00	1.65	1.35	0.0400	-0.040
Q4+LI (PG)	0.1946	0.205	0.401	4.03	1.70	1.44	0.0404	-0.038
Exact	0.1950	0.210	0.400	4.00	1.65	1.35	0.0400	-0.040

5.3. Stress concentration around a circular hole

To analyse the influence of the micropolar effect in a homogeneous and isotropic linear elastic solid, the so-called Kirsch problem [41] – an infinite plate with a circular hole subject to uniform tension – is considered next. We focus on the so-called *stress-concentration factor* (K_t) – the ratio between a maximum longitudinal stress at the edge of the hole and the applied surface loading. The classical theory predicts a constant stress concentration factor equal to three regardless of the hole size and the material parameters. Experimental tests, e.g. [7], however, indicate a smaller stress-concentration factor than that. The analytical solution of the problem using the micropolar theory [6], however, is dependent on the hole radius r, the coupling number N and the characteristic

length l of the material and it returns the stress-concentration factor which is increasingly smaller than the one obtained by the classical theory as the diameter of the hole decreases.

In our numerical analysis, the plate is necessarily taken to be of a finite size and only a quarter of the plate is analysed. The square quarter is taken to be of unit thickness, $L = 16.2$ mm long and with a hole of radius $r = 0.216$ mm subject to uniform uniaxial tension $p = 1$ N/mm^2 acting on one of its undented sides. The micropolar material parameters $\mu = 76923.1$ N/mm^2, $\lambda = 115385.0$ N/mm^2, $\beta = \gamma = 6352.25$ N, which correspond to the modulus of elasticity $E = 200000$ N/mm^2, Poisson's ratio $n = 0.3$ and a characteristic length $l = r/1.063 = 0.2031984948$ m are taken from [37]. The value of the micropolar material parameter ν is varied (indicating a variation in the coupling number N). The normal displacements and the microrotations along the dented sides are restrained.

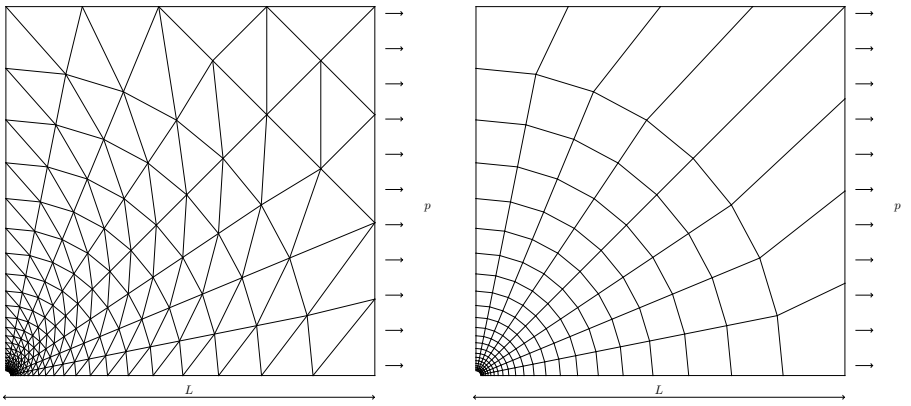

(a) Triangular elements (b) Quadrilateral elements

Figure 5: Finite-element mesh for the Kirsch problem

The results obtained by the proposed triangular and quadrilateral elements with linked interpolation are compared to those obtained by the finite elements with standard Lagrangian interpolation. The finite element meshes for trian-

gular and quadrilateral elements, shown in Figure 5, consist of 360 and 176 elements, respectively, and are generated using software GMSH [42]. In the structured part of the mesh the finite elements project radially from the hole and are embedded within 22 concentric circles propagating in geometric progression with ratio between the radial increments of 1.2. The part of the mesh between the outermost band of the elements between the concentric circles and the undented edges is defined manually. The input file for GMSH can be found in the Appendix A.

The stresses are observed in the element containing the stress-concentration point P=(0.0, 0.216), where the analytical solution is provided. To avoid extrapolation of the computed stresses, the stress values for the numerical simulation are given at Gauss points closest to the edge of the hole, not at the exact edge, thus they can never exactly match the analytical result. For easier comparison with [37] the chosen integration for all triangular elements is 7 Gauss integration points per element, which brings us closer to the edge, where the analytical solution and Providas's solutions are given. Considering quadrilateral finite elements, the minimum order of integration needed is used, i.e. 3×3 for order 1 elements, 4×4 for order 2 elements and 5×5 for order 3 elements. The Gauss points monitored have the co-ordinates equal to GP1=(0.00251643, 0.243476), GP2=(0.0199002, 0.218483) and GP3=(0.0198966, 0.21843) for the triangular elements, and GP4=(0.0048953, 0.222164), GP5=(0.00300768, 0.220075) and GP6=(0.00201581, 0.218758) for the rectangular elements. The results for the stresses obtained using the triangular and the quadrilateral elements are shown in Tables 4 and 5, respectively.

Table 4: Triangular elements: Stress-concentration factor K_t

N	ν	K_t, [6]	Element	K_t, GP1	Element	K_t, GP2	Element	K_t, GP3
0.0	0.0	3.00	T3	2.846	T6	2.865	T10	2.849
			T3+LI (PG)	2.846	T6+LI	2.897	T10+LI (PG)	2.849
0.25	5130.77	2.849	T3	2.737	T6	2.729	T10	2.715
			T3+LI (PG)	2.740	T6+LI	2.729	T10+LI (PG)	2.715
0.50	25 638.5	2.555	T3	2.508	T6	2.466	T10	2.454
			T3+LI (PG)	2.514	T6+LI	2.466	T10+LI (PG)	2.454
0.75	98 900.0	2.287	T3	2.267	T6	2.228	T10	2.219
			T3+LI (PG)	2.273	T6+LI	2.228	T10+LI (PG)	2.219
0.90	327 938.0	2.158	T3	2.101	T6	2.117	T10	2.108
			T3+LI (PG)	2.109	T6+LI	2.117	T10+LI (PG)	2.108

The numerical results for all the elements show that with the micropolar effect increased (through the coupling number N) the stress-concentration factor is reduced, as predicted theoretically. The predictive power of all the elements, however, decreases as the coupling number increases.

Table 5: Quadrilateral elements: Stress-concentration factor K_t

N	ν	K_t, [6]	Element	K_t, GP4	Element	K_t, GP5	Element	K_t, GP6
0.0	0.0	3.00	Q4	2.904	Q9	2.911	Q16	2.916
			Q4+LI (PG)	2.904	Q9+LI (PG)	2.911	Q16+LI (PG)	2.916
0.25	5130.77	2.849	Q4	2.768	Q9	2.769	Q16	2.774
			Q4+LI (PG)	2.769	Q9+LI (PG)	2.769	Q16+LI (PG)	2.774
0.50	25 638.5	2.555	Q4	2.496	Q9	2.492	Q16	2.498
			Q4+LI (PG)	2.497	Q9+LI (PG)	2.492	Q16+LI (PG)	2.498
0.75	98 900.0	2.287	Q4	2.236	Q9	2.240	Q16	2.248
			Q4+LI (PG)	2.236	Q9+LI (PG)	2.240	Q16+LI (PG)	2.248
0.90	327 938.0	2.158	Q4	2.104	Q9	2.119	Q16	2.129
			Q4+LI (PG)	2.104	Q9+LI (PG)	2.119	Q16+LI (PG)	2.129

With the higher-order elements of both the triangular and the quadrilateral type, the linked-interpolation elements' behaviour is in this example exceedingly close to that of the standard elements, i.e. these elements do not contribute to the faster convergence rate. Interestingly, the higher-order linked-interpolation element T6+LI does behave marginally better than its Lagrangian counterparts when there is no micropolar effect present. With the low-order triangular elements, the linked-interpolation slightly improves the accuracy, this time however with an increasing micropolar effect. This behaviour is not observed in the low-order quadrilateral elements, though. Finally, as in [37], it is observed that in the triangular elements, depending on the value of the micropolar effects, the higher-order elements often produce results of lower accuracy than the low-order elements. This effect, however, is not observed in the quadrilateral elements.

By refining the finite element mesh in the vicinity of the hole, we expect to get closer to the analytical solution. In order to demonstrate this, the problem is additionally solved using Q4+LI (PG) by retaining the same number of elements, but by increasing the ratio between the radial increments in the mesh.

The ratios are chosen as 1.5 and 1.8 and the results for stresses are observed in Gauss points GP7 = (0.00475192, 0.215653) and GP8 = (0.00474938, 0.215536) and presented in Table 6.

Table 6: Quadrilateral element Q4+LI (PG): Stress-concentration factor K_t for meshes of different densities around the hole

N	K_t, [6]	ratio = 1.2	ratio = 1.5	ratio = 1.8
		K_t, GP4	K_t, GP7	K_t, GP8
0.0	3.00	2.904	2.922	2.992
0.25	2.849	2.769	2.785	2.849
0.50	2.555	2.497	2.512	2.562
0.75	2.287	2.236	2.257	2.291
0.90	2.158	2.104	2.128	2.152

5.4. A cantilever beam subject to pure bending

In an attempt to determine the micropolar material constants experimentally, the analytical solution for stresses, displacements and microrotations of a micropolar elastic plate subject to pure bending has been derived by Gauthier [15]. His solution has assumed the lateral boundary conditions which prevent anticlastic distortion, in effect turning the problem into pure plane-strain bending of a rectangular micropolar specimen.

Let Gauthier's specimen be of thickness b and height h placed in the xy plane with x as its axis of centroids and assume an applied loading resulting in an in-plane bending moment M acting on the sides of the specimen orthogonal to the x-axis. While in the classical elasticity the only way to subject the specimen to pure bending is via a linearly varying normal surface traction $p_{sx} = \frac{2y}{h} p_0$, Gauthier has shown that in the micropolar continuum the state of pure bending requires *both* such a traction *and* a constant surface moment m_{sz} acting on the

same sides of the specimen, *with a unique relationship between them* given as

$$\frac{m_{sz}}{p_0} = \frac{1}{h}\frac{(\lambda+2\mu)(\beta+\gamma)}{2\mu(\lambda+\mu)} \equiv \frac{h}{6}(1-n)\delta, \tag{46}$$

with Poisson's coefficient n and $\delta = 24(l_b/h)^2$. Obviously, for a material with vanishing characteristic length ($l_b \to 0$) the state of pure bending may not be achieved if the surface moment loading is present, while for a general micropolar material such a state is only possible when m_{sz} and p_0 are given in the proportion defined above resulting in $M = p_0 W_z + m_{sz} A$ with $A = bh$ and $W_z = bh^2/6$. As a result,

$$p_0 = \frac{1}{1+(1-n)\delta}\frac{M}{W_z}, \quad m_{sz} = \frac{(1-n)\delta}{1+(1-n)\delta}\frac{M}{A}, \tag{47}$$

the only non-vanishing stress components are

$$\sigma_{xx} = -\frac{1}{1+\delta}\frac{M}{W_z}\frac{2y}{h}, \quad \mu_{zx} = \frac{(1-n)\delta}{1+\delta}\frac{M}{A}. \tag{48}$$

and, for the specimen fixed at the origin of the co-ordinate system, the displacement and rotation fields are

$$\varphi = \frac{1}{1+\delta}\frac{Mx}{bD}, \quad u = -\frac{1}{1+\delta}\frac{Mxy}{bD}, \quad v = \frac{1}{2}\frac{1}{1+\delta}\frac{M}{bD}\left(x^2 + \frac{n}{1-n}y^2\right), \tag{49}$$

where $D = \frac{Eh^3}{12(1-n^2)}$ is the flexural rigidity. This problem does not induce any non-symmetry in the stress tensor field, i.e. the solution does not depend on the coupling number N (and therefore also on the material parameter ν). For $l_b \to 0$, the classical solution is approached in all fields.

The solution demonstrates that all fields are obtained from their respective values in classical elasticity as *multiplied by the factor* $\frac{1}{1+\delta}$, i.e. bending stiffness in micropolar elasticity increases with an increase in the material characteristic length l_b. In engineering terms, bending resistance is not anymore proportional to the height of the specimen squared and we say that the micropolar elasticity exhibits the so-called *size effect* with the solution increasingly departing from the

classical solution when the characteristic length reaches the order of magnitude of a representative dimension of the specimen.

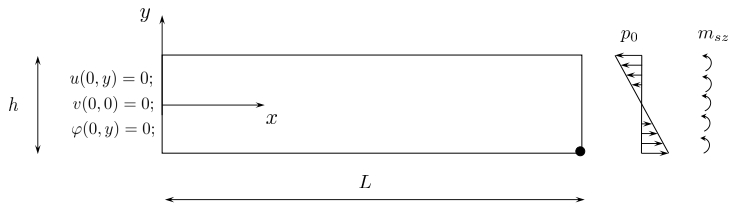

Figure 6: Cantilever beam subject to pure bending

The problem described (see Figure 6) is analysed using quadrilateral and triangular elements of different order, using both the proposed linked interpolation and the Lagrangian interpolation. The problem is solved for different values of the characteristic length $l_b \sim \sqrt{\beta+\gamma}$. The resultant bending moment $M = 20$ Nm is applied through a linearly varying surface loading and a constant surface moment as described above and summarised in Table 7. The distributed loading is applied through corresponding concentrated nodal forces and moments obtained by integration as defined in equation (22).

Table 7: External loading depending on the value of l_b

l_b/h	l_b	$\beta+\gamma$	p_0	m_{sz}
0.05	0.1	24.0	28.708 133 971 291 860	0.430 622 009 569 378
0.15	0.3	216.0	21.352 313 167 259 780	2.882 562 277 580 070
0.30	0.6	864.0	11.450 381 679 389 320	6.183 206 106 870 228
0.60	1.2	3 456.0	4.010 695 187 165 778	8.663 101 604 278 070
0.90	1.8	7 776.0	1.925 545 571 245 185	9.358 151 476 251 610

The length of the cantilever is taken as $L = 10$ m, the height is $h = 2$ m and the engineering material parameters are $E = 1500$ N/m^2 and $n = 0.25$ which give the Lamé constants $\mu = 600$ N/m^2 and $\lambda = 600$ N/m^2. The material

parameter $\nu = 200\ \mathrm{N/m^2}$ depends on the value of the coupling number, which is, in this example, chosen to be equal to $N = 0.5$, but in this example can have an arbitrary value, as discussed above. Along the left-hand edge of the cantilever all the horizontal displacements and microrotations are restrained. The vertical displacement at the left-hand edge is restrained only at the cantilever axis in order to preserve the symmetry of the system.

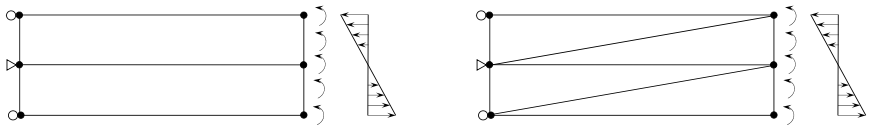

(a) Q4 elements (b) T3 elements

Figure 7: Finite element mesh, loading and boundary conditions

The problem is solved using a mesh of two quadrilateral or four triangular elements of different order shown in Figure 7. The left-hand side nodes in the higher-order elements are restrained in the same way as the corner nodes. The results for the vertical displacement and microrotation v and φ at the bottom right-hand node and the stress σ_{xx} in the Gauss point nearest to this node obtained by the quadrilateral elements Q4 are compared to the analytical solution in Table 8 and Figure 8, while the same results obtained by the triangular elements T3 are shown in Table 10 and Figure 9.

Table 8: Results obtained using two quadrilateral elements (Q4), 3x3 integration points, GP = (8.887298, -0.887298), A – Analytical solution, N – Numerical solution

Element	l_b/h	A v	N v	A φ	N φ	A $\sigma_{xx,GP}$	N $\sigma_{xx,GP}$
Q4	0.05	0.90012	0.06892	0.17943	0.01269	25.47267	2.22127
Q4+LI (PG)			0.87402		0.17426		26.08884
Q4	0.15	0.66948	0.06740	0.13345	0.01296	18.94586	2.08130
Q4+LI (PG)			0.65566		0.13071		19.56450
Q4	0.30	0.35902	0.06203	0.07157	0.01261	10.15990	1.88150
Q4+LI (PG)			0.35518		0.07082		10.59720
Q4	0.60	0.12575	0.04624	0.02507	0.00978	3.55870	1.29741
Q4+LI (PG)			0.12527		0.02498		3.73716
Q4	0.90	0.06037	0.03234	0.01204	0.00691	1.70853	0.89668
Q4+LI (PG)			0.06025		0.01202		1.79747

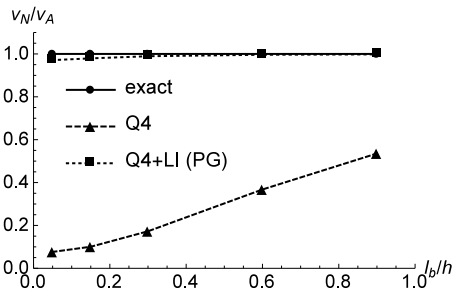

(a) End node vertical displacements

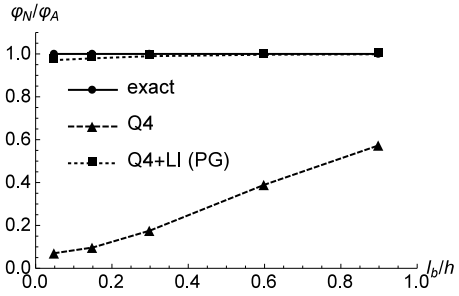

(b) End node microrotation

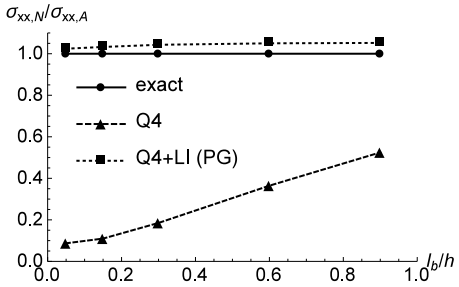

(c) Stresses in Gauss point

Figure 8: Cantilever beam subject to pure bending - Q4 elements

We can see that Q4+LI (PG) significantly improves the results of the conventional Lagrange Q4 element, in particular for the problems with exisiting, but less pronounced, micropolar effect. The higher-order quadrilateral elements with Lagrangian interpolation as well as those with Petrov-Galerkin linked interpolation exactly reproduce the analytical solution.

The improvement due to the linked interpolation in low-order triangulars is also present but it is far less significant than in the low-order quadrilaterals. The higher-order triangulars with both the Lagrangian interpolation as well as those with the Petrov-Galerkin linked interpolation again provide the analytical result. When the Petrov-Galerkin interpolation in six-node triangulars is switched off (note that in these elements the Petrov-Galerkin interpolation is not necessary for convergence), the results deteriorate by at most 0.025% (for $l_b/h = 0.05$),

the errors reducing rapidly as l_b/h increases and falling to below 0.003% for $l_b/h = 0.30$.

Next we analyse h-convergence of the first-order elements with Lagrange and linked interpolation by modelling the same problem shown in Figure 6 for low $l_b/h = 0.05$ and high $l_b/h = 0.90$ micropolar effects. We perform the analysis on a number of meshes with equal number of uniform elements per length and height of the specimen and show the results in Table 9. We can see that Q4+LI (PG) has a faster convergence rate than the Q4 element, but both elements converge to the exact solution. Again the comparative advantage of the linked-interpolation elements is more obvious for the lower value of l_b/h.

Table 9: h-convergence of first order quadrilateral elements for $l_b/h = 0.05$ and $l_b/h = 0.9$, 3×3 integration points used

Element	Mesh size	$l_b/h = 0.05$		$l_b/h = 0.9$	
		v	φ	v	φ
Q4	2×2	0.22336	0.04233	0.04976	0.01010
Q4+LI (PG)		0.87402	0.17426	0.06024	0.01201
Q4	4×4	0.51163	0.09735	0.05730	0.01148
Q4+LI (PG)		0.89340	0.17803	0.06034	0.01203
Q4	16×16	0.85921	0.16939	0.06017	0.01200
Q4+LI (PG)		0.89970	0.17933	0.06037	0.01203
Q4	32×32	0.88951	0.17666	0.06032	0.01203
Q4+LI (PG)		0.90001	0.17940	0.06037	0.01204
Q4	64×64	0.89744	0.17871	0.06036	0.01203
Q4+LI (PG)		0.90009	0.17942	0.06037	0.01204
Q4	128×128	0.89945	0.17924	0.06037	0.01203
Q4+LI (PG)		0.90011	0.17942	0.06037	0.01204
Q4	256×256	0.89995	0.17938	0.06037	0.01204
Q4+LI (PG)		0.90012	0.17943	0.06037	0.01204
EXACT		0.90012	0.17943	0.06037	0.01204

Table 10: Results obtained using four triangular elements (T3), 7 integration points, GP=(5.29858, -0.9402841), A – Analytical solution, N – Numerical solution

Element	l_b/h	A v	N v	A φ	N φ	A $\sigma_{xx,GP}$	N $\sigma_{xx,GP}$
T3	0.05	0.90012	0.02359	0.17943	0.00542	26.9938	0.7583
T3+LI (PG)			0.07463		0.01737		3.6797
T3	0.15	0.66948	0.02518	0.13345	0.00586	20.0772	0.7166
T3+LI (PG)			0.08089		0.01765		2.8406
T3	0.30	0.35902	0.02645	0.07157	0.00650	10.7666	0.6447
T3+LI (PG)			0.08296		0.01807		2.5249
T3	0.60	0.12575	0.02367	0.02507	0.00604	3.7712	0.5156
T3+LI (PG)			0.05967		0.01307		1.7067
T3	0.90	0.06037	0.01891	0.01204	0.00487	1.8106	0.3993
T3+LI (PG)			0.03844		0.00844		1.0842

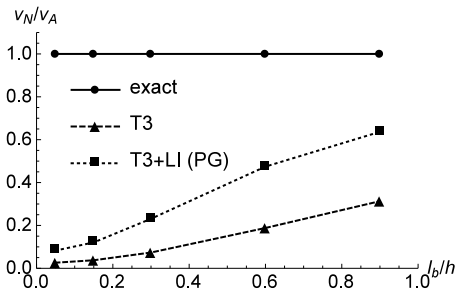

(a) End node vertical displacements

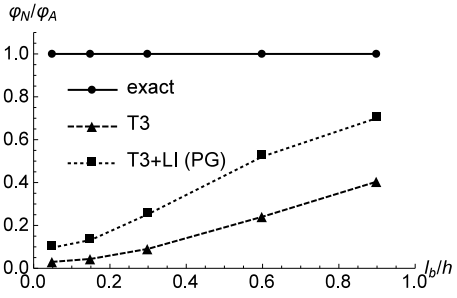

(b) End node microrotation

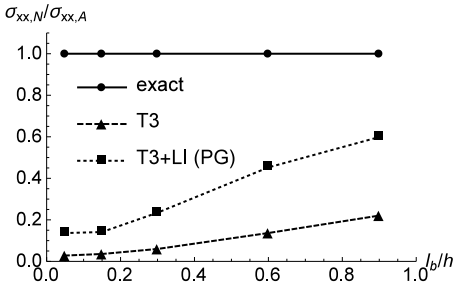

(c) Stresses in Gauss point

Figure 9: Cantilever beam subject to pure bending - T3 elements

As for the quadrilaterals, the h-refinement is also performed for the triangular elements of first order with Lagrange and linked interpolation. Even though the contribution of linked interpolation is small, from Table 11 we can see that it contributes to faster convergence rate.

Table 11: h-convergence of first order triangular elements for $l_b/h = 0.05$ and $l_b/h = 0.9$, 7 integration points used

Element	Mesh size	$l_b/h = 0.05$		$l_b/h = 0.9$	
		v	φ	v	φ
T3	2×2×2	0.00882	0.01817	0.03656	0.00813
T3+LI (PG)		0.20132	0.04242	0.04976	0.01040
T3	4×4×2	0.26903	0.05235	0.05162	0.01058
T3+LI (PG)		0.48812	0.09885	0.05705	0.01151
T3	16×16×2	0.78363	0.15460	0.05974	0.01193
T3+LI (PG)		0.85617	0.17057	0.06015	0.01200
T3	32×32×2	0.86781	0.17232	0.06022	0.01205
T3+LI (PG)		0.88874	0.17709	0.06032	0.01203
T3	64×64×2	0.89181	0.17755	0.06033	0.01203
T3+LI (PG)		0.89725	0.17883	0.06036	0.01203
T3	128×128×2	0.89803	0.17895	0.06036	0.01203
T3+LI (PG)		0.89940	0.17927	0.06037	0.01203
T3	256×256×2	0.89960	0.17930	0.06037	0.01203
T3+LI (PG)		0.89994	0.17939	0.06037	0.01204
EXACT		0.90012	0.17943	0.06037	0.01204

6. Conclusion

A new family of membrane finite elements interpolated using the linked-interpolation concept for the analysis of the micropolar continuum theory is presented. Triangular and quadrilateral elements of different order are developed and tested through four numerical examples and compared to the conventional elements interpolated using the Lagrangian interpolation. In order to assure convergence, the proposed linked-interpolation finite elements are modified using Petrov-Galerkin interpolation. In the pure-bending test it is shown

that, for the low-order elements, the linked interpolation makes the solution more accurate, significantly so for the case of the Q4 quadrilaterals. Interestingly, this improvement is reduced as the ratio between the characteristic length of the micropolar material and a characteristic specimen dimension increases. For the infinite plate with circular hole benchmark problem, the newly proposed finite elements correctly reproduce the amount of stress concentration predicted by the micropolar theory, but they are only marginally more accurate than their Lagrangian counterparts.

Acknowledgement - The research presented in this paper has been financially supported by the Croatian Science Foundation grants *Configuration-dependent Approximation in Non-linear Finite-element Analysis of Structures* (HRZZ-IP-11-2013-1631), *Young Researchers' Career Development Project – Training of Doctoral Students* and the French Government scholarship.

References

[1] W. Nowacki, Theory of micropolar elasticity, Springer-Verlag, Vienna, 1972.

[2] R. S. Lakes, Size effects and micromechanics of a porous solid, Journal of Materials Science 18 (1983) 2572–2580. doi:10.1007/BF00547573.

[3] A. C. Eringen, Microcontinuum Field Theories: I. Foundations and Solids, Springer-Verlag, New York, 2012.

[4] E. Cosserat, F. Cosserat, Théorie des corps déformables, Herman, Paris, 1909.

[5] L. E. Malvern, Introduction to the mechanics of a continious medium, Prentice-Hall, Inc, New Jersey, 1969.

[6] H. Neuber, On the general solution of linear-elastic problems in isotropic and anisotropic Cosserat continua, Springer Berlin Heidelberg, Berlin, Heidelberg, 1966, pp. 153–158. doi:10.1007/978-3-662-29364-5_16.

[7] L. Toubal, M. Karama, B. Lorrain, Stress concentration in a circular hole in composite plate, Composite Structures 68 (1) (2005) 31–36. doi:10.1016/j.compstruct.2004.02.016.

[8] W. Voigt, Theoretische studien über die elasticitätsverhältnisse der krystalle, Abhandlungen der Königlichen Gesellschaft der Wissenschaften zu Göttingen 34 (1887) 3–51.

[9] W. Günther, Zur Statik und Kinematik des Cosseratschen Kontinuums, Abhandlungen der Braunschweigischen Wissenschaftlichen Gesellschaft 10 (1958) 195–213.

[10] R. A. Toupin, Theories of elasticity with couple-stress, Archive for Rational Mechanics and Analysis 17 (2) (1964) 85–112. doi:10.1007/BF00253050.

[11] H. Schäfer, Das Cosserat kontinuum, ZAMM - Journal of Applied Mathematics and Mechanics 47 (8) (1967) 485–498. doi:10.1002/zamm.19670470802.

[12] A. C. Eringen, Linear Theory of Micropolar Elasticity, Journal of Mathematics and Mechanics 15 (1966) 909–923. doi:10.2307/24901442.

[13] J. Dyszlewicz, Micropolar Theory of Elasticity, Springer-Verlag Berlin and Heidelberg GmbH & Co. KG, Berlin, 2004. doi:0.1007/978-3-540-45286-7.

[14] V. Eremeyev, L. Lebedev, H. Altenbach, Foundations of Micropolar Mechanics, Springer-Verlag, Berlin, 2013. doi:10.1007/978-3-642-28353-6.

[15] R. Gauthier, W. E. Jahsman, A Quest for Micropolar Elastic Constants, Journal of Applied Mechanics 42 (2) (1975) 369–374. doi:10.1115/1.3423583.

[16] J. F. C. Yang, R. S. Lakes, Transient Study of Couple Stress Effects in Compact Bone: Torsion, Journal of Biomechanical Engineering 103 (4) (1981) 275–279. doi:10.1115/1.3138292.

[17] J. F. C. Yang, R. S. Lakes, Experimental study of micropolar and couple stress elasticity in compact bone in bending, Journal of Biomechanics 15 (2) (1982) 91–98. doi:10.1016/0021-9290(82)90040-9.

[18] R. S. Lakes, S. Nakamura, J. C. Behiri, W. Bonfield, Fracture mechanics of bone with short cracks, Journal of Biomechanics 23 (10) (1990) 967–975. doi:10.1016/0021-9290(90)90311-P.

[19] W. B. Anderson, R. S. Lakes, Size effects due to Cosserat elasticity and surface damage in closed-cell polymethacrylimide foam, Journal of Materials Science 29 (24) (1994) 6413–6419. doi:10.1007/BF00353997.

[20] Z. Rueger, R. S. Lakes, Cosserat elasticity of negative Poisson's ratio foam: experiment, Smart Materials and Structures 25 (5) (2016) 054004. doi:10.1088/0964-1726/25/5/054004.

[21] R. S. Lakes, Experimental Microelasticity of two porous solids, International Journal of Solids and Structures 22 (1) (1986) 55–63. doi:10.1016/0020-7683(86)90103-4.

[22] C. P. Chen, R. S. Lakes, Holographic study of conventional and negative Poisson's ratio metallic foams: elasticity, yield and micro-deformation, Journal of Materials Science 26 (20) (1991) 5397–5402. doi:10.1007/BF02403936.

[23] Z. Bažant, M. Christensen, Analogy between micropolar continuum and grid frameworks under initial stress, International Journal of Solids and Structures 8 (3) (1972) 327–346. doi:10.1016/0020-7683(72)90093-5.

[24] X. L. Wang, W. J. Stronge, Micropolar theory for two-dimensional stresses in elastic honeycomb, Proceedings of the Royal Society A, Mathematical, Physical and Engineering Sciences 455 (1986) (1999) 2091–2116. doi:10.1098/rspa.1999.0394.

[25] R. J. Mora, A. M. Waas, A. Arbor, Evaluation of the Micropolar elasticity constants for honeycombs, Acta Mechanica 192 (2007) 1–16. doi:10.1007/s00707-007-0446-8.

[26] D. Besdo, Towards a Cosserat-theory describing motion of an originally rectangular structure of blocks, Archive of Applied Mechanics 80 (1) (2010) 25–45. doi:10.1007/s00419-009-0366-2.

[27] S. Hassanpour, G. R. Heppler, Micropolar elasticity theory: a survey of linear isotropic equations, representative notations, and experimental investigations, Mathematics and Mechanics of Solids (2015) 1–19.doi:10.1177/1081286515581183.

[28] G. Jelenić, E. Papa, Exact solution of 3D Timoshenko beam problem using linked interpolation of arbitrary order, Archive of Applied Mechanics 81 (2) (2011) 171–183. doi:10.1007/s00419-009-0403-1.

[29] D. Ribarić, G. Jelenić, Higher-order linked interpolation in quadrilateral thick plate finite elements, Finite Elements in Analysis and Design 51 (2012) 67–80. doi:10.1016/j.finel.2011.10.003.

[30] D. Ribarić, G. Jelenić, Higher-order linked interpolation in triangular thick plate finite elements, Engineering Computations 31 (1) (2014) 69–109. doi:10.1108/EC-03-2012-0056.

[31] H. Jeffreys, On isotropic tensors, Mathematical Proceedings of the Cambridge Philosophical Society 73 (1) (1973) 173–176. doi:10.1017/S0305004100047587.

[32] R. S. Lakes, Physical Meaning of Elastic Constants in Cosserat, Void, and Microstretch Elasticity, Mechanics of Materials and Structures 11 (3) (2016) 1–13. doi:10.2140/jomms.2016.11.217.

[33] A. Tessler, S. Dong, On a hierarchy of conforming Timoshenko beam elements, Computers & Structures 14 (3-4) (1981) 335–344. doi:10.1016/0045-7949(81)90017-1.

[34] F. Auricchio, R. Taylor, A shear deformable plate element with an exact thin limit, Computer Methods in Applied Mechanics and Engineering 118 (3-4) (1994) 393–412. doi:10.1016/0045-7825(94)90009-4.

[35] A. Ibrahimbegović, Nonlinear Solid Mechanics: Theoretical Formulations and Finite Element Solution Methods, Springer, London, 2009.

[36] O. C. Zienkiewicz, R. L. Taylor, The Finite Element Method Volume 1 : The Basis, Butterworth-Heinemann, Oxford, 2000.

[37] E. Providas, M. A. Kattis, Finite element method in plane Cosserat elasticity, Computers and Structures 80 (27-30) (2002) 2059–2069. doi:10.1016/S0045-7949(02)00262-6.

[38] E. L. Wilson, A. Ibrahimbegović, Use of incompatible displacement modes for the calculation of element stiffnesses or stresses, Finite Elements in Analysis and Design 7 (3) (1990) 229–241. doi:10.1016/0168-874X(90)90034-C.

[39] M. A. Wheel, A control volume-based finite element method for plane micropolar elasticity, International Journal for Numerical Methods in Engineering 75 (8) (2008) 992–1006. doi:10.1002/nme.2293.
URL http://doi.wiley.com/10.1002/nme.2293

[40] H. Zhang, H. Wang, G. Liu, Quadrilateral isoparametric finite elements for plane elastic Cosserat bodies, Acta Mechanica Sinica 21 (4) (2005) 388–394. doi:10.1007/s10409-005-0041-y.

[41] E. Kirsch, Die Theorie der Elastizität und die Bedürfnisse der Festigkeitslehre, Zeitschrift des Vereines deutscher Ingenieure 42 (1898) 797–807.

[42] C. Geuzaine, J.-F. Remacle, Gmsh: a three-dimensional finite element mesh generator with built-in pre- and post-processing facilities, International Journal for Numerical Methods in Engineering 79 (11) (2009) 1309–1331. doi:10.1002/nme.2579.

Appendices

A. Input file to generate the FE mesh for the plate with hole problem

GMSH software package

```
// Gmsh project created on Wed Sep 27 21:48:45 2017
// Sara Grbcic, sara.grbcic@uniri.hr

L=16.2; //domain length and height
r=0.216; //hole radius
a = 1.2; // ratio between the radial increments
n=22; // number of divisions
p=(a-1)/(a^(n)-1)*(L-r);
alpha=90/8*Pi/180; // angle in radians to obtain boundary nodes

Point(1) = {0, 0, 0, 0};
Point(2) = {r, 0, 0, 0};
Point(3) = {0, r, 0, 0};


j=4;
k=1;

For i In {0:n-1}

Point(j) = {r+p*(1-a^i)/(1-a), 0, 0, 0};
Point(j+1) = {0, r+p*(1-a^i)/(1-a), 0, 0};

Circle(k) = {j-1, 1, j-2};
Transfinite Line {k} = 9;

Line (k+1) ={j-2,j};
Transfinite Line {k+1} = 2;

Circle(k+2) = {j, 1, j+1};
Transfinite Line {k+2} = 9;

Line (k+3) ={j+1,j-1};
Transfinite Line {k+3} = 2;

Line Loop (k+4)={k,k+1,k+2,k+3};

Plane Surface (k+5) = {(k+4)};

Transfinite Surface {k+5} = {j-2,j,j+1,j-1} Right;

p1=k;
p2=j;
j=j+2;
k=k+5;

EndFor


// THE OTHER STRUCTURED PART
// SURFACE 1
Point(2*n+4) = {L, 0, 0, 0};
```

```
// Gmsh project created on Wed Sep 27 21:48:45 2017
// Sara Grbcic, sara.grbcic@uniri.hr

L=16.2; //domain length and height
r=0.216; //hole radius
a = 1.2; // ratio between the radial increments
n=22; // number of divisions
p=(a-1)/(a^(n)-1)*(L-r);
alpha=90/8*Pi/180; // angle in radians to obtain boundary nodes

Point(1) = {0, 0, 0, 0};
Point(2) = {r, 0, 0, 0};
Point(3) = {0, r, 0, 0};


j=4;
k=1;

For i In {0:n-1}

Point(j) = {r+p*(1-a^i)/(1-a), 0, 0, 0};
Point(j+1) = {0, r+p*(1-a^i)/(1-a), 0, 0};

Circle(k) = {j-1, 1, j-2};
Transfinite Line {k} = 9; // 9 = number of nodes per line

Line (k+1) ={j-2,j};
Transfinite Line {k+1} = 2;  // 2 = number of nodes per line

Circle(k+2) = {j, 1, j+1};
Transfinite Line {k+2} = 9;  // 9 = number of nodes per line

Line (k+3) ={j+1,j-1};
Transfinite Line {k+3} = 2;

Line Loop (k+4)={k,k+1,k+2,k+3};

Plane Surface (k+5) = {(k+4)};

Transfinite Surface {k+5} = {j-2,j,j+1,j-1} Right;
Recombine Surface {k+5};

p1=k;
p2=j;
j=j+2;
k=k+5;

EndFor


// THE OTHER STRUCTURED PART
// SURFACE 1
```

```
Point(2*n+4) = {L, 0, 0, 0};
Line (5*n+2) = {p2,2*n+4};
Transfinite Line {5*n+2} = 2;

Point(2*n+5) = {L, L, 0, 0}; //101
Point(2*n+6) = {L, (r+p*(1-a^(n-1))/(1-a))*Sin(alpha), 0, 0};
Point(2*n+7) = {L, (r+p*(1-a^(n-1))/(1-a))*Sin(2*alpha), 0, 0};
Point(2*n+8) = {L, (r+p*(1-a^(n-1))/(1-a))*Sin(3*alpha), 0, 0};
Line (5*n+3) = {2*n+4,2*n+6,2*n+7,2*n+8,2*n+5};
Transfinite Line {5*n+3} = 5;

Point(2*n+9) = {(r+p*(1-a^(n-1))/(1-a))*Cos(4*alpha),
(r+p*(1-a^(n-1))/(1-a))*Sin(4*alpha), 0, 0};
Line (5*n+4) = {2*n+5,2*n+9};
Transfinite Line {5*n+4} = 2;

Circle (5*n+5) = {2*n+9,1,p2};
Transfinite Line {5*n+5} = 5;

Line Loop(5*n+6)={5*n+2,5*n+3,5*n+4,5*n+5};

Plane Surface (5*n+7) = {5*n+6};
Transfinite Surface {5*n+7};
Recombine Surface {5*n+7};

// SURFACE 2
Point(2*n+10) = {0, L, 0, 0};
Line (5*n+8) = {2*n+5,2*n+10};
Transfinite Line {5*n+8} = 5;

Line (5*n+9) = {2*n+10,p2+1};
Transfinite Line {5*n+9} = 2;

Circle (5*n+10) = {p2+1,1,2*n+9};
Transfinite Line {5*n+10} = 5;

Line Loop(5*n+11)={5*n+8,5*n+9,5*n+10,-(5*n+4)};

Plane Surface (5*n+12) = {5*n+11};
Transfinite Surface {5*n+12};
Recombine Surface {5*n+12};

Mesh.Algorithm = 1;

Mesh.ElementOrder = 1; //Set element order


//Physical Surface("quads") = {66, 210, 205, 111, 106, 101, 96, 91, 86, 81, 76,
71, 11, 61, 56, 51, 46, 41, 36, 31, 26, 21, 16}; //This needs to be done
manually

Mesh 2;  // Generate 2D mesh
```

```
Coherence Mesh;  // Remove duplicate entities

//Save "plate-with-hole-Q4-a=1.2.msh";  // Save mesh in MSH format
```